



Cite this: DOI: 10.1039/c5cp05522a

# A simulation study of the electrostriction effects in dielectric elastomer composites containing polarizable inclusions with different spatial distributions

Elshad Allahyarov,<sup>\*abcd</sup> Hartmut Löwen<sup>a</sup> and Lei Zhu<sup>b</sup>

Controlled actuation of electroactive polymers with embedded high dielectric nanoparticles is theoretically analyzed. If the inclusions are placed randomly in the elastomer body, the composite always contracts along the direction of the applied field. For a simple cubic distribution of inclusions, contraction occurs if the applied field is directed along the [001] direction of the lattice. For inclusions occupying the sites of other lattice structures such as body-centered or face-centered cubic crystals, the composite elongates along the field direction if it is applied along the [001] direction. The stability of the elongation against the imperfectness of the lattice site positions and the distortion ratio of the initial structures are examined. Finite elongation windows show up for the initially distorted body-centered cubic and face-centered cubic crystals as a function of the distortion ratio of the initial structure. The existence of these elongation windows are also predicted from the analysis of the electrostatic energy of the distorted body-centered cubic and face-centered cubic lattice structures. Our results indicate that the electrostriction effect, which is the main contribution to the actuation of low aspect-ratio composites, strongly depends on the geometry of the spatial distribution of nanoparticles, and can thereby largely be tuned.

Received 15th September 2015,  
Accepted 12th November 2015

DOI: 10.1039/c5cp05522a

www.rsc.org/pccp

## 1 Introduction

Electroactive polymers and composites having tunable actuation properties belong to the fast growing field of smart materials with promising applications in many directions.<sup>1–5</sup> Initially being developed for sensors and shock adsorbers, these materials are now viewed as perfect building blocks for artificial muscles,<sup>6,7</sup> drug delivery systems,<sup>8,9</sup> and nano-cancer applications.<sup>10</sup>

These electroactive materials, also called electro- or magneto-sensitive elastomers, are composites with 3-0 connectivity,<sup>11,12</sup> where the index 3 refers to the 3-dimensional self-connectivity of the primary active phase which is inert to polarization, and the index 0 refers to the non-connected, *i.e.* isolated, secondary passive phase which is highly polarizable. The composites consist of a flexible host polymer matrix impregnated with

hard-core inclusions. Usually, the host matrix is a dielectric elastomer with the Young's modulus in the range of 0.1–20 MPa, and low dielectric permittivity in the range between 2 and 7. The inclusions are polarizable spheres with high dielectric permittivity and a diameter ranging between several hundreds of nm to several  $\mu\text{m}$ . Until recently the research on electroactive composites was mostly focused on enhancing the Maxwell contraction of the host matrix through modifying their dielectric and elastic properties.<sup>13–25</sup> The increase of the effective dielectric constant of the composite makes the Maxwell pressure stronger. Also, the local field effects between neighboring inclusions induce an additional contraction of the composite along the applied field direction.

During the last decade considerable theoretical advances have been made on elucidating the role of the inclusion's spatial distribution and the composite's initial shape on its actuation.<sup>26–32</sup> It was revealed that the composite with a particular type of inclusion distribution might experience an elongation strain. Theoretical studies of the composite actuation distinguish two separate contributions to the composite strain: a macroscopic electrostatic effect (*i.e.*, atomic or vibrational polarization with elongated molecular bonds) as obtained within a continuum mechanics approach, and the effects based on the explicit accounting for the dipolar interactions

<sup>a</sup> Institut für Theoretische Physik II, Weiche Materie, Heinrich-Heine Universität Düsseldorf, Universitätsstrasse 1, 40225 Düsseldorf, Germany

<sup>b</sup> Department of Macromolecular Science and Engineering, Case Western Reserve University, Cleveland, Ohio 44106-7202, USA.  
E-mail: elshad.allahyarov@case.edu

<sup>c</sup> Theoretical Department, Joint Institute for High Temperatures, Russian Academy of Sciences (ITAN), 13/19 Izhor'skaya street, Moscow 125412, Russia

<sup>d</sup> International Research Centre, Baku State University, Baku, Azerbaijan

between the discrete inclusions on the mesoscopic length scale. The first contribution always results in the elongation of the composite along the applied field direction, and is a nonlinear function of the aspect ratio of the composite. The aspect ratio here is defined as the ratio of the composite dimensions  $a/b$ , where  $a$  is the composite thickness along the applied field, and  $b$  is its width across the applied field. At small and high aspect ratios  $a/b$ , corresponding to the prolate and oblate material geometries, the macroscopic electrostatic elongation effect is weak, whereas at the intermediate aspect ratios it is strong. The second contribution to the composite strain, called the electrostriction effect, however, results in a negative contribution to the composite strain along the applied field direction. A sum of these two contributions for some inclusion's spatial distributions gives rise to a finite window of elongation<sup>28,30–32</sup> as a function of the aspect ratio of the composite. That window, however, might be completely screened by the Maxwell contraction term, which acts on the host polymer regardless of the dipole moment of particles and their distribution factors.

The electrostriction effect has been discussed in many experimental studies.<sup>33–42</sup> Under the poling fields up to  $20 \text{ MV m}^{-1}$  contracting strains up to 10% were observed whereas the Maxwell-stress induced strain of the pure polymer was below 1%. In other studies single-walled carbon nanotubes<sup>38–41</sup> and lead zirconate titanate (PZT) ceramics<sup>42</sup> were used as fillers in electrostrictive polymers where a weak electrostriction effect of few percents was reported. Recent studies report on the electrostriction properties of carbon black (CB) nanoparticles in polyurethane (PU) elastomers.<sup>36,37</sup> At dilute concentrations of CB and low fields,  $\eta \approx 0.01$  and  $E < 4 \text{ MV m}^{-1}$ , a twice larger than the Maxwell strain was reported, though the nature of this enhanced strain is debated to come from the dielectric permittivity increase in the CB-polymer mixtures.

In all existing theoretical studies, the magnitude of the linear response coefficients and the sign of the composite actuation are predicted for a frozen particle distribution, meaning that the particle displacement in the course of deformation is not taken into account. However, in reality, the latter, together with the shape change of the composite during the deformation, contributes to the depolarization factor, and through it to the ultimate strain of the composite. These effects are hard to include in a theoretical analysis, but can readily be incorporated into a computer simulation of the composite actuation which resolves the nature of the inclusions explicitly. Composite simulations use different representations for the host matrix polymer: it can be modeled as a full atomistic material, or a coarse grained polymer with several of its atoms grouped into blobs, or a low level coarse-grained polymer consisting of elastic springs between the inclusions. In this paper, we use the latter model which allows for the simulation of large systems.

The goal of this study is to explicitly evaluate the electrostriction effect of inclusions and its dependence on the inclusion's spatial distribution. For the latter we consider four different distributions: a simple cubic (SC), a body centered cubic (BCC), a face centered cubic (FCC) periodic lattice, and a random

distribution. In order to decouple the electrostriction effect from the macroscopic electrostatic effect we assume that the full system has a low aspect-ratio (such as a slab). As shown in ref. 28, in this case, the macroscopic contribution to the strain becomes negligibly small, and only the electrostriction and Maxwell strains need to be considered.

We use a mesoscopic spring-bead model for the composite combining classical phenomenological electrostatics on the mesoscopic length scale of the inclusions with phenomenological elasticity theory, but the effective polarization-induced (dipole–dipole-like) interactions between the inclusions are taken explicitly into account. Within this model the response of the composite to external fields is calculated by using the method of equality of internal pressure components in all three directions. The pressure components are determined from the virials of the elastic and electrostatic forces. Our method presents a new approach to the actuation modeling of bulk composite. Assuming that the full shape of the sample has a low aspect ratio, and thus ignoring the electrostatic effects, we investigate the electrostriction related contributions to the composite strain. Within our spring-bead model we derive an analytical expression for the Young's modulus. We show that the strain of the composite along the applied field strongly depends on the distribution of inclusions inside the host matrix. Whereas the composites with homogeneously (randomly) distributed inclusions always contract along the applied field, the actuation of regular lattice composites depends on their lattice structure: the SC composite shrinks along the applied field, but the BCC and FCC composites show a net elongation response along the applied field oriented parallel to the [001] direction of the lattice. This elongation is shown to depend on the defects of the inclusion distribution and on the distortion ratio of the initial structures. For the BCC and FCC lattices we detect the existence of an elongation window as a function of the distortion ratio of the initial structure. We show that a similar elongation window can be predicted from the analysis of the electrostatic energy of the distorted crystal.

The remaining part of the paper is organized as follows. In Section 2 we give the underlying theory of the composite polarization and discuss the origins of the macroscopic electrostatic and electrostriction contributions to the composite actuation. In subsection 2.4 we calculate the free energy of the composite deformation used to tune the elasticity parameter of our simulation model. Details of our simulation set-up and the spring-bead model for the composite are given in Section 3. In Section 4 we give the details of our simulation method for the calculation of the composite strain as a response to the applied field. Simulation results for the composite strain in different fields and for different starting configurations for the inclusion's distribution are collected in Section 5. We show that the composite actuation and the contribution from the electrostriction strongly depend on the spatial distribution of inclusions. In Section 6 we give guidelines for experimental realization of theoretical predictions for the composite actuation. Finally we conclude in Section 7.

## 2 Theoretical model

### 2.1 General theory of macroscopic electrostatics of composites

We consider a composite membrane consisting of a host matrix with dielectric permittivity  $\epsilon_m$  impregnated with  $N$  polarizable inclusions with permittivities  $\epsilon_p$ . As a general case we assume that the dielectrics have arbitrary shapes as shown in Fig. 1, where only a single inclusion is pictured. The case of spherical inclusions in a slab-shaped host matrix will be considered in Section 2.2 as a particular case of the configuration shown in Fig. 1. When the host matrix is polarized under the external field  $\vec{E} \parallel \vec{z}$ , the projection of the total field inside the inclusion on the  $z$ -axis is

$$\vec{E}_p = \vec{E}_m - \frac{\vec{P}_p}{\epsilon_0 \epsilon_m} \alpha_p^z + \sum_j \vec{E}_j \quad (1)$$

where the first term,  $\vec{E}_m$ , is the projection of the total field inside the host matrix on the  $z$ -axis,

$$\vec{E}_m = \vec{E} - \frac{\vec{P}_m}{\epsilon_0} \alpha_m^z \quad (2)$$

The second terms in eqn (1) and (2) describe the dielectric depolarization effects along the  $z$  axis stemming from the induced charges at the dielectric boundaries in the direction of the  $z$ -axis. Here  $\vec{P}_p$  and  $\vec{P}_m$  are the projections of the particle and host matrix polarizations on the  $z$ -axis correspondingly. The third term in eqn (1) is the projection of the electrical field contribution from the dipolar fields of other inclusions  $j$  ( $1 \leq j \leq N$ ), existing in the host matrix, on the  $z$ -axis.

The depolarization factors  $0 < \alpha_k^z < 1$ , ( $k = m, p$ ) in eqn (1) and (2) depend on the dielectric geometries measured in terms of their aspect ratios  $\zeta_k = a_k/b_k$  along the field  $\vec{E}$ , where  $a_k$  and  $b_k$  are the averaged dielectric sizes in the field and lateral directions correspondingly.<sup>43</sup> For simple geometries such as a slab

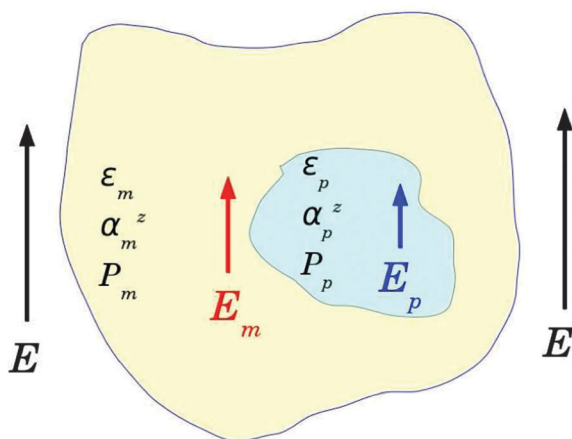


**Fig. 1** Schematic representation explaining the polarization of a dielectric inclusion in a host dielectric polymer under the field  $\vec{E}$  oriented parallel to the  $z$ -axis. Along the field direction the dielectrics have dielectric permittivities  $\epsilon_k$ , depolarization factors  $\alpha_k^z$ , and induced polarizations  $P_k$ , where  $k = p$  for inclusions, and  $k = m$  for the host polymer.

with  $\zeta = 0$  (an infinite slab placed perpendicular to the applied field  $\vec{E}$ ), or a cylinder with  $\zeta \rightarrow \infty$  (an infinite cylinder placed along the applied field  $\vec{E}$ ), or a sphere with  $\zeta = 1$ , the depolarization factor  $\alpha_k^z$  takes values 1, 0, and 1/3 respectively. As has been shown in ref. 28, in the case of regular lattice sites used for particle distributions, the depolarization factors  $\alpha_k^z$  can be modified to include also the electrostriction effects. The resulting depolarization field then can take both positive and negative values. Because our aim is to consider only the behavior of the electrostriction effects in low aspect-ratio membranes, for which the electrostatic effects are believed to be weak, there is no need to modify the depolarization terms in eqn (1) and (2).

The setup in Fig. 1 corresponds to a constant surface charge condition on the electrode surface which implies an open circuit case. This boundary condition differs from short circuit conditions, which are used in most experimental studies. For low inclusion volume fractions  $\eta$  not exceeding several percents, when the contribution of the inclusion polarization to the host matrix polarization is small and thus can be neglected,  $\vec{P}_m$  is defined as

$$\vec{P}_m = \epsilon_0(\epsilon_m - 1)\vec{E}_m \quad (3)$$

Combining eqn (2) with eqn (3), for the field  $\vec{E}_m$  and the polarization  $\vec{P}_m$  we get

$$\vec{E}_m = \frac{\vec{E}}{1 + (\epsilon_m - 1)\alpha_m^z} \quad (4)$$

$$\vec{P}_m = \frac{\epsilon_0(\epsilon_m - 1)\vec{E}}{1 + (\epsilon_m - 1)\alpha_m^z} \quad (5)$$

The polarization of the inclusion  $\vec{P}_p$  has two parts: the first part  $\vec{P}_1 = \epsilon_0(\epsilon_p - 1)\vec{E}_p$  corresponds to the polarization of inclusion placed into the vacuum, and the second part  $\vec{P}_2'$  is the polarization created by the host matrix inside an empty cavity of the inclusion shape,

$$\vec{P}_p = \vec{P}_1 + \vec{P}_2' \quad (6)$$

The term  $\vec{P}_2'$  can be replaced by the polarization of the inclusion with permittivity  $\epsilon_m$  placed into the vacuum,  $\vec{P}_2' = -\vec{P}_2 = -\epsilon_0(\epsilon_m - 1)\vec{E}_p$ . Therefore, eqn (6) becomes

$$\vec{P}_p = \epsilon_0(\epsilon_p - \epsilon_m)\vec{E}_p \quad (7)$$

From eqn (1) and (7) for the polarization  $\vec{P}_p$  we get,

$$\vec{P}_p = \frac{\epsilon_p - \epsilon_m}{\epsilon_m + (\epsilon_p - \epsilon_m)\alpha_p^z} \epsilon_0 \epsilon_m \left( \frac{1}{1 + (\epsilon_m - 1)\alpha_m^z} \vec{E} + \sum_j \vec{E}_j \right) \quad (8)$$

This simple expression for  $P_p$  defines its dependence on the inclusion and host polymer geometries along the  $z$ -axis through the coefficients  $\alpha_k^z$ ,  $k = m, p$  for the matrix and the particle, respectively.

The induced dipole moment of the inclusion along the  $z$ -axis has two parts,

$$\vec{\mu}_p = V_p \vec{P}_p = \vec{\mu}_p^0(E) + \vec{\mu}_p^j(E_j) \quad (9)$$

where the first part  $\vec{\mu}_p^0$  is the pure dipole moment stemming from the external field  $\vec{E}$ ,

$$\vec{\mu}_p^0 = V_p \frac{\epsilon_p - \epsilon_m}{\epsilon_m + (\epsilon_p - \epsilon_m)\alpha_p^z} \frac{1}{1 + (\epsilon_m - 1)\alpha_m^z} \epsilon_0 \epsilon_m \vec{E} \quad (10)$$

and the second part  $\vec{\mu}_p(E_j)$  is the excess dipole moment corresponding to the cumulative sum of the fields created by other inclusions  $j$  ( $1 \leq j \leq N$ ) at the position of the inclusion  $i$ ,

$$\vec{\mu}_p^i = V_p \frac{\epsilon_p - \epsilon_m}{\epsilon_m + (\epsilon_p - \epsilon_m)\alpha_p^z} \epsilon_0 \epsilon_m \sum_j^N \vec{E}_j \quad (11)$$

Here  $V_p$  is the inclusion volume (for spherical inclusions  $V_p = 4\pi R^3/3$ ,  $R = \sigma/2$ , where  $\sigma$  is the inclusion diameter). The free energy  $F_d$  of a single dipole  $\vec{\mu}_p^0$  in the external field  $\vec{E}$ , which is the energy needed to polarize a single inclusion along the  $z$ -axis, is defined as

$$F_d = - \int_0^E \mu_p^0 dE' = - \frac{1}{2} V_p \frac{\epsilon_p - \epsilon_m}{\epsilon_m + (\epsilon_p - \epsilon_m)\alpha_p^z} \frac{\epsilon_0 \epsilon_m E^2}{1 + (\epsilon_m - 1)\alpha_m^z} \quad (12)$$

From this expression we see that low  $F_d$  values, which are necessary for achieving equilibrium polarized states, correspond to smaller depolarization factors  $\alpha_p^z$  and  $\alpha_m^z$ . In other words, the macroscopic electrostatics effect indicates the feasibility of the composite elongation along the applied field  $\vec{E}$ . This effect depends on the initial shape aspect ratio  $a/b$  of the host matrix and has been analyzed for ferrogels and magnetosensitive elastomers in ref. 28, 31 and 32.

For the field  $E_p$  inside the inclusion, combining eqn (1) and (7) we get

$$E_p = E \frac{3}{\epsilon_p + 2\epsilon_m} = E_m \frac{3\epsilon_m}{\epsilon_p + 2\epsilon_m} \quad (13)$$

This field is smaller than  $E_m$  for  $\epsilon_p > \epsilon_m$ . The partial expulsion of  $E_m$  from the interior of the high dielectric constant particle increases the macroscopic field in the vicinity of the inclusion. As a result, at high inclusion volume fractions, the average macroscopic field  $E_m$  in the host matrix should be modified to account for such local field effects,  $\tilde{E}_m = E_m(1 + \gamma\eta)$  with some scaling coefficient  $\gamma$ . In the current setup with  $\eta \ll 1$ , local field effects are considered negligible.

## 2.2 Electrostriction effects in slab-shaped composites with spherical inclusions

Electrostriction effects in composite materials are defined by the dipole-dipole interaction forces  $\vec{F}_{ji}$  and by the torques  $\vec{\tau}_i$  of the electrostatic fields. For a slab-shaped host matrix and spherical inclusions, putting  $\alpha_m^z = 1$ , and  $\alpha_p^z = 1/3$ , into eqn (9)–(11), for the dipole moment of inclusions we get

$$\vec{\mu}_p^i = 4\pi\epsilon_0 R^3 \frac{\epsilon_p - \epsilon_m}{\epsilon_p + 2\epsilon_m} \left( \vec{E} + \sum_j^N \epsilon_m \vec{E}_j(\mu_j) \right) \quad (14)$$

Consequently, the polarization of the inclusion is

$$\alpha_p = 4\pi\epsilon_0 R^3 \frac{\epsilon_p - \epsilon_m}{\epsilon_p + 2\epsilon_m} \quad (15)$$

Obviously, eqn (14) cannot be used for other host polymer matrix shapes considered in ref. 30, 32 and 44. For the host polymer having a spherical geometry the dipole moment  $\vec{\mu}_p^i$  will be

$$\vec{\mu}_p^i = 4\pi\epsilon_0 R^3 \frac{\epsilon_p - \epsilon_m}{\epsilon_p + 2\epsilon_m} \left( \frac{3\epsilon_m}{\epsilon_m + 2} \vec{E} + \sum_j^N \epsilon_m \vec{E}_j(\mu_j) \right) \quad (16)$$

with an additional prefactor  $3\epsilon_m/(\epsilon_m + 2)$  for the applied field  $E$ . Consequently, the polarization of the inclusion will also change to

$$\alpha_p = 4\pi\epsilon_0 R^3 \frac{\epsilon_p - \epsilon_m}{\epsilon_p + 2\epsilon_m} \frac{3\epsilon_m}{\epsilon_m + 2} \quad (17)$$

In other words, the polarization of inclusions depends on the geometry of the host matrix.

The induced electric field  $\vec{E}_i(\mu_p^i)$  of the inclusion  $i$ ,

$$\vec{E}_i(\mu_p^i) = \frac{1}{4\pi\epsilon_0\epsilon_m r_{ij}^3} \left( \frac{3}{r_{ij}^2} \left( (\vec{\mu}_p^i \cdot \vec{r}_{ij}) \vec{r}_{ij} - \vec{\mu}_p^i \right) \right) \quad (18)$$

defines the electrostatic force  $\vec{F}_{ij}$  between a pair of interacting inclusions

$$\begin{aligned} \vec{F}_{ji} &= \frac{1}{4\pi\epsilon_0\epsilon} \frac{3}{r_{ji}^5} \\ &\times \left( (\vec{\mu}_j \cdot \vec{\mu}_i) \vec{r}_{ji} - 5 \frac{(\vec{\mu}_i \cdot \vec{r}_{ji})(\vec{\mu}_j \cdot \vec{r}_{ji})}{r_{ji}^2} \vec{r}_{ji} + (\vec{\mu}_j \cdot \vec{r}_{ji}) \vec{\mu}_i + (\vec{\mu}_i \cdot \vec{r}_{ji}) \vec{\mu}_j \right) \end{aligned} \quad (19)$$

where  $\vec{r}_{ji} = \vec{r}_i - \vec{r}_j$ .

The orientation of dipoles is controlled by the torque created by the fields  $\vec{E}$  and  $\vec{E}_j$ ,

$$\vec{\tau}_i = \vec{\mu}_i \times \vec{E} + \vec{\mu}_i \times \sum_j^N \vec{E}_j \quad (20)$$

For the case of induced dipoles, the second term in eqn (20) is weak compared to the first term,  $\sum_j^N E_j/E \approx (8\epsilon_m r^3)^{-1}$ , where  $r$  denotes the distance between the inclusions scaled to their diameter  $\sigma$ .

It should be noted that whereas the electrostatic effects described by eqn (12) always result in the composite elongation along the field direction, there is no clear understanding on how the electrostriction effects described by eqn (19) and (20) contribute to the composite deformation. Obviously the reorientation and rearrangement of induced dipoles depend on the morphology of their spatial distribution in the host matrix.

For the case of induced dipoles  $\vec{\mu}_i \parallel \vec{\mu}_j \parallel \vec{E}$  the pair interaction potential between dipoles reduces to

$$V_{ij} = \frac{\mu_i \mu_j}{4\pi\epsilon_0\epsilon_m r_{ij}^3} (1 - 3\cos^2(\theta)) \quad (21)$$

The strength of the electrostriction is measured by the coupling parameter  $\Gamma$ ,

$$\Gamma = \frac{|V_{ij}(r_p)|}{k_B T} \quad (22)$$

where  $r_p$  is the nearest neighbor distance between the dipoles,  $r_p = (3/(4\pi\rho_p))^{1/3}$ , with  $\rho_p = \eta/V_p$  being the density of inclusions. For the case of induced dipoles homogeneously distributed in the host matrix, a modified coupling parameter is introduced,

$$\Gamma = \left\langle \frac{\mu_i \mu_j}{4\pi\epsilon_0\epsilon_m r_p^3} \left| \frac{1 - 3\cos^2(\theta)}{k_B T} \right| \right\rangle_\theta = \frac{\mu_i \mu_j}{8\pi\epsilon_0\epsilon_m k_B T r_p^3} \quad (23)$$

where the angular brackets are for the averaging over all mutual dipolar configurations. In the strong electrostriction regime  $\Gamma > 1$  the dipoles “connect” to each other through their chaining along the field direction (this is the case for electro-rheological fluids). In the extreme regime  $\Gamma \gg 1$  the chains form a secondary structure by forming 2D lattices in the lateral direction. A formation of such connected dipolar structures results in the host polymer matrix deformation.

### 2.3 Maxwell pressure and mixing rules

The actuation of the composite elastomer, together with the electrostatic and electrostriction forces described above, has also a contribution from the Maxwell pressure

$$p = P_m E \quad (24)$$

which always contracts the composite in the field direction. Using eqn (3) and (4), the pressure  $p$  is rewritten as

$$p = \epsilon_0 E^2 \left( 1 - \frac{1}{\epsilon_m} \right) \quad (25)$$

and the resulting Maxwell strain  $\Sigma_M$  of the composite under the open circuit conditions is

$$\Sigma_M = -\frac{p}{Y} = -\frac{\epsilon_0 E^2}{Y} \left( 1 - \frac{1}{\epsilon_m} \right) \quad (26)$$

where  $Y$  is Young's elastic modulus of the host matrix. It should be noted that eqn (26) is derived from linear elasticity theory for host matrix deformations, hence it is applicable only to the cases of small strains  $\Sigma_z < 0.1$  (in percentages this corresponds to the strain values less than 10%). For moderate strains,  $0.1 \leq \Sigma_z \leq 0.2$ , a modified expression for the strain, instead of eqn (26), should be used, see ref. 16. Under the constant voltage boundary (or short circuit) conditions with a reduced applied field  $E/\epsilon_m$  (in order to keep the total field in the inclusion the same as in the open circuit case), eqn (25) and (26) take forms

$$p^{(V)} = D_m E_m = \epsilon_0 \epsilon_m E_m^2 \quad (27)$$

and

$$\Sigma_M^{(V)} = -\frac{p^{(V)}}{Y} = -\frac{\epsilon_0 E^2}{\epsilon_m Y} \quad (28)$$

The ratio of these two strains is

$$\frac{\Sigma_M}{\Sigma_M^{(V)}} = \epsilon_m - 1 \quad (29)$$

If the host matrix permittivity is  $\epsilon_m = 1$ , its Maxwell strain vanishes,  $\Sigma_M = 0$ , because no polarization appears on the host matrix surface facing the vacuum. However, under constant voltage conditions, the attraction between oppositely charged electrodes will squeeze the composite resulting in a nonzero strain  $\Sigma_M^{(V)}$ . For the particular case  $\epsilon_m = 2$  the two strains are equal to each other.

When the host matrix contains inclusions, the parameters  $Y$  and  $\epsilon_m$  in eqn (26), and also in eqn (28) should be treated as effective constants  $\tilde{Y}$  and  $\tilde{\epsilon}_m$  derived from the mixing rules. By using the Maxwell-Garnett equation for the spherical inclusions at the volume fraction  $\eta = NV_p/V_m$ , for the  $\tilde{\epsilon}_m$  we get<sup>45-48</sup>

$$\tilde{\epsilon}_m = \epsilon_m \frac{2\epsilon_m + \epsilon_p - 2\eta(\tilde{\epsilon}_m - \epsilon_p)}{2\epsilon_m + \epsilon_p + \eta(\tilde{\epsilon}_m - \epsilon_p)} \quad (30)$$

The effective Young's modulus of the composite can be approximated by the Einstein's mixing rule<sup>24,49-51</sup>

$$\tilde{Y} = Y + Yk_1\eta + Yk_2\eta^2 \quad (31)$$

with  $k_1 = 2.5$  and  $k_2 = 14.1$ .

### 2.4 Free energy of elastic deformations of the host polymer matrix

The strength of the composite deformation as a reaction to the electrostatic, electrostriction and Maxwell forces is defined primarily by the Young's modulus  $Y$  of the host matrix. Under the incompressibility conditions the composite with initial dimensions  $L_x^0$ ,  $L_y^0$ , and  $L_z^0$ , attains new dimensions  $L_x$ ,  $L_y$ , and  $L_z$  with  $V_m = L_x L_y L_z = L_x^0 L_y^0 L_z^0$ . In the limit of small strains the free energy of the deformation is

$$F_d = \frac{1}{2} \left( \frac{G_x A_{yz}}{L_x^0} \Delta L_x^2 + \frac{G_y A_{xz}}{L_y^0} \Delta L_y^2 + \frac{G_z A_{xy}}{L_z^0} \Delta L_z^2 \right) \quad (32)$$

Here  $G_k$  for  $k = x, y, z$  are the shear moduli of the matrix,  $A_{ij} = L_i^0 L_j^0$  for  $i, j = x, y, z$  and  $i \neq j \neq k$  is the surface area of the non-deformed composite perpendicular to the deformation direction  $k$ , and  $\Delta L_i = L_i - L_i^0$  is the deformation along the axis  $i$ . We note that eqn (32) is valid for a network of randomly jointed chains in the limit of small chain extensions  $d \ll nd_0$ , where  $d$  is the chain end-to-end distance,  $n$  is the number of joints for each chain in the host matrix,  $d_0$  is the bond length between neighboring joints, and  $nd_0$  is the maximum extensibility of the chain. The probability of  $d$  for randomly jointed chains with rigid bonds  $d_0$  is given by the Gaussian distribution function.<sup>52,53</sup> Within the Gaussian statistics the force-extension  $f(d)$  relation for a single chain follows the Hookian-like linear relation  $f^*(d^*) = 3d^*$ , where  $f^*$  is a rescaled elastic force  $f^* = f(d)d_0/(k_B T)$ , and  $d^* = d/(nd_0)$  is a rescaled chain extension. For a more realistic representation of the elastic properties of the host matrix for the whole range of chain extensions, the Langevin chain statistics<sup>52-54</sup> should be used. Within this

approximation the entanglement of polymer chains are taken into account by various network models, which are generally based on the non-linear force-extension dependence  $f^*(d^*) = L^{-1}(d^*)$ . Here  $L^{-1}(x)$  denotes the inverse Langevin function.<sup>52</sup> The Gaussian chain statistics can be derived from the Langevin chain statistics if the first linear term of the Taylor expansion for  $d^*$  is retained. The addition of higher order terms of  $d/d_0$  in the Langevin statistics results in higher elastic forces for the same chain extension  $d^*$ . These elastic forces are usually approximated by the finitely extensible nonlinear elastic (FENE) model.<sup>55–57</sup> In this paper we will use the Gaussian chain statistics for its simplicity for the calculation of the host matrix free energy. A calculation of the host matrix's strain energy for different network entanglement models can be found in ref. 53 and 54.

Assuming an isotropy for the shear modulus components,  $G_x = G_y = G_z = G$ , and rewriting  $\Delta L_i^2 / (L_i^0)^2 = l_i^2 + 2(1 - l_i) - 1$  where  $l_i = L_i / L_i^0$ , eqn (32) for the free energy of elastic deformations per unit volume becomes

$$f_d = \frac{F_d}{V_0} = \frac{G}{2} \left( \sum_j^{x,y,z} l_i^2 - 3 + 2 \sum_j^{x,y,z} \Sigma_i \right) \quad (33)$$

Here the strain of the matrix is defined as  $\Sigma_i = l_i - 1$ . Eqn (33) can be further simplified taking into account  $l_z = 1/(l_x l_y)$ ,

or  $1 + \Sigma_z = \frac{1}{(1 + \Sigma_x)^2} \approx 1 - 2\Sigma_x$ , and thus  $\Sigma_x = \Sigma_y = -\Sigma_z/2$ .

Therefore we have

$$f_d = \frac{G}{2} \left( \sum_j^{x,y,z} l_i^2 - 3 - \Sigma_x - \Sigma_y + 2\Sigma_z \right) = \frac{G}{2} \left( \sum_j^{x,y,z} l_i^2 - 3 \right) \quad (34)$$

The shear modulus  $G$  and the Young's modulus  $Y$  of the composite are related as

$$Y = 2G(1 + \nu) \quad (35)$$

where  $\nu$  is Poisson's ratio. Assuming a rubber-like elasticity for the host polymer, and putting  $\nu \approx 0.5$  into eqn (35), we get  $Y = 3G$ . For the free energy of the elastic deformation per unit volume we have

$$f_d = \frac{Y}{6} \left( \sum_i l_i^2 - 3 \right) \quad (36)$$

This elastic energy will be used to predict the elastic constant  $\chi$  of the spring-bead based simulation model.

### 3 Simulation model for composites

The elasticity of the host polymer matrix can be modeled at different coarse-grained levels. At the highest level of coarse-graining a full-atomistic model with a well-defined force-field for the host polymer can be used. At the medium level of coarse-graining several host polymer atoms are grouped into blobs for which the partial charges and modified force field parameters are necessary to develop. Finally, within the lowest level coarse-graining the host matrix is replaced by effective

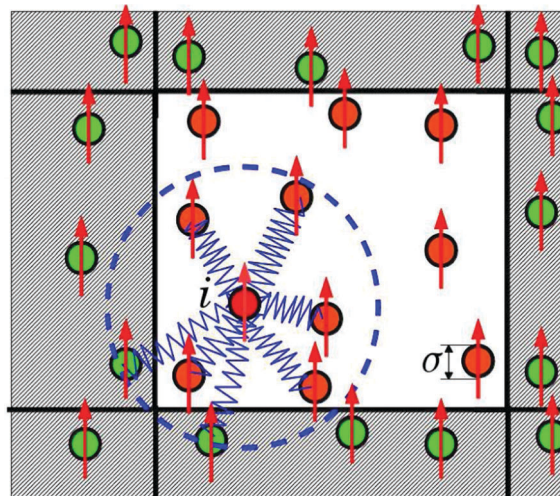


Fig. 2 Schematic representation explaining our simulation model. For clarity a 2D simulation cell is shown. The inclusions of diameter  $\sigma$  are shown in red in the main cell, and in green in the periodic images of the main cell, which are shown as a hatched area. Each inclusion is connected to  $n_b$  nearest neighbors by springs: for clarity this is shown just for one inclusion  $i$  in the center of a circle (blue in online) which encloses  $n_b = 7$  neighbors. The inclusions have induced dipole moments  $\vec{\mu}$  shown as red arrows. Each inclusion electrostatically interacts with all inclusions in the main cell, and with all their images in neighboring cells (note that only a part of periodic images are shown).

elastic springs connecting some selective nodes of the polymer. In this case the elastic constant of springs needs to be tuned for matching the Young's modulus of the coarse-grained model to the Young's modulus of the full atomistic model, or to the real material. The lowest level of coarse-graining allows us to simulate the actuation of larger systems consisting many inclusions with diameters in the range between  $\sigma = 100$  nm and  $\sigma = 100$   $\mu$ m.

In the following we consider  $N$  hard sphere inclusions spatially distributed in the bulk of the host matrix of volume  $V_m$ . The homogeneous distribution of inclusions is created by their random insertion into the host polymer matrix. For the non-homogeneous distribution of inclusions they are placed at the regular lattice sites. Such regular composites, depending on the type of the lattice structure, are referred as the SC, BCC, and FCC composites. Each inclusion is connected by elastic springs to its  $n_b$  nearest neighbors, as shown in Fig. 2. The resulting dipole-spring model was also recently used in the context of ferroelectrics.<sup>58–60</sup> For the regular lattice composites the nearest neighbors are chosen from the closest coordination shells. For the random composite the nearest neighbors are taken from the list of the first  $n_b$  closest particles.

All springs are assumed to have the same elasticity constant  $\chi$ . The lattice structure of the inclusion distribution is periodically extended in all three directions. It should be noted that our simulation model in the limit of  $\chi \rightarrow 0$  decouples the elastic and electrostatic interactions allowing to go to the regime of electro-rheological liquids.

When an external field  $\vec{E}$  is applied along the  $z$ -axis, which coincides with the  $[001]$  direction of the lattice structures, the

long-range interaction between the induced dipoles is handled using Ewald's summation technique<sup>61–63</sup> with a correction for the rectangular shape of the simulation cell.<sup>64</sup> Test simulations with direct summations over the 100 neighboring image cells produced results similar to Ewald's summation with a difference between these two methods less than 0.01%. Direct summation of the dipolar interactions can also be speeded up using the dipole–(infinite)chain and (infinite)chain–(infinite)chain interaction potentials.<sup>65</sup>

Our set-up corresponds to simulating the bulk volume of the host matrix, assuming that the system boundaries in the [001] direction are far away. Omitting the boundaries is necessary for getting a true long-range electrostatic contribution to the dipole–dipole interactions between the inclusions. Therefore, considering a bulk system with periodically repeated images in all three directions makes it possible to get reliable actuation results with a modest number (up to 10 000) of inclusions in the system. The option of taking the system boundaries explicitly into account demands excessive simulation efforts. For example, a composite elastomer of volume 1 mm<sup>3</sup>, with particles of diameter  $\sigma = 200$  nm distributed in its volume at very low volume fraction  $\eta = 0.005$ , hosts almost  $10^{10}$  inclusions. Simulation of such huge amounts of dipoles even on parallelized clusters is an utterly time consuming process.

It should be noted that in the 3–0 composite materials initially poled under sufficiently strong fields, heterocharges and homocharges can be trapped at the interface between the dielectric inclusions and the elastomer matrix. Such trapping basically results in the enhancement of the piezoelectric coefficient of composite materials.<sup>66–72</sup> In our set-up the role of trapped charges, as a first approximation, can be comprehended through the calculation of the remnant dipole moment  $\bar{\mu}_i$  of the particle-charges complex under a zero field  $E = 0$ . In the following,  $\bar{\mu}_i$  should be added to the induced dipole moments  $\bar{\mu}_p^i(E)$  of inclusions given by eqn (14). This will result in the shifting of  $\Sigma_z(E)$ ,<sup>70–72</sup> and in the hysteresis of the polarization-field curve.<sup>73</sup> For realizing the precise role of the trapped charges, a more sophisticated model should be used, which is not the scope of this work.

Another issue is the altered characteristics of the polymer matrix in the vicinity of particles because of the particle-polymer bonding. Within the particle-polymer interphase both the dielectric permittivity  $\epsilon_m$  and the Young's modulus  $Y_m$  of the polymer have enhanced values compared to their bulk values.<sup>74</sup> Therefore, a more appropriate core-shell particle model is required for the correct calculation of the 3–0 composite actuation.<sup>75</sup> However, the difference between the core-shell and bare-core (used in the current work) models is expected to be negligible when the surface-to-surface distance between neighboring inclusions is much larger than the doubled shell thickness. If this condition is met, and also provided that the volume fraction of the shell is much smaller than  $\eta$ , the shell region effectively can be considered as a part of the inclusion volume. Otherwise, the core-shell model should be strictly implemented.<sup>76</sup> For  $\eta \approx 0.01$  used in the current set-up, and for particles of radius  $R = 100$  nm, the average surface-to-surface

distance between neighboring particles is about 600–1000 nm, which is at least two orders of magnitude larger than the typical shell thickness of a few (2–5) nanometers. Therefore, for the current set-up the bare-core particle model can be assumed as a reliable approximation. Additionally, the non-polar nature of the host matrix blocks the polarization gradient from the inclusions into the host matrix,<sup>74</sup> which makes the changes to the computed electrostriction effects negligible.

### 3.1 Evaluation of the Young's modulus of the host polymer matrix from simulations

The elasticity parameter  $\chi$  of the spring-bead model invoked in our simulations defines the Young's modulus of the simulated system. To get a good matching between the simulation predicted Young's modulus and the Young's modulus of the real composite material, we run a few test simulations with different fitting prefactors  $\chi$ . The simulated energy of elastic deformations per unit volume is

$$K = \frac{1}{2V} \sum_i^{x,y,z} \chi \Delta r_{ij}^2 \quad (37)$$

Here  $\Delta r_{ij} = |\vec{r}_{ij} - \vec{r}_{ij}^0|$  is the bond length deformation between the inclusions  $i$  and  $j$ . Then, equating the energy  $K$  to the energy of elastic deformations given in eqn (36), we identify the correct  $\chi$  for which the simulation predicted Young's modulus

$$Y_{MD} = \frac{3\chi}{V} \frac{\sum_i^{x,y,z} \Delta r_{ij}^2}{\sum_i^{x,y,z} l_i^2 - 3} \quad (38)$$

is equal to the composite modulus  $Y$ ,  $Y_{MD} = Y$ .

A guess value for the parameter  $\chi$  can be roughly estimated using the following analytical procedure. At small strains, assuming that all free energy components in eqn (32) are the same, and accepting  $G = 3Y$ , for the free energy of elastic deformations we get

$$F_d = \frac{YV}{2} (\Sigma_z)^2 \quad (39)$$

Thus, the energy per inclusion is

$$f_N^z = \frac{F_d}{N} = \frac{Y}{2\rho_p} (\Sigma_z)^2 \quad (40)$$

This energy is equal to the spring energy between a pair of dipoles  $i$  and  $j$ ,

$$E_{\text{elastic}} = \frac{1}{2}\chi(r_{ij} - r_{ij}^0)^2 = \frac{1}{2}\chi(\Sigma_z)^2 (r_{ij}^0)^2 \quad (41)$$

Hence, from eqn (40) and (41), and using the nearest-neighbor distance  $r_{ij}^0 = \left(\frac{3}{4\pi\rho_p}\right)^{1/3}$ , for the effective spring constant we have

$$\chi = \frac{Y}{\rho_p (r_{ij}^0)^2} = \frac{4\pi}{3} Y \rho_p^0 \quad (42)$$

Test simulations with  $\chi$  predicted by eqn (42) produced  $Y_{MD} \approx Y$  within an accuracy of 3%. Hence, the knowledge of  $r_{ij}^0$  is enough for getting a fairly good guess for the spring constant of our spring-bead model. We also note that for the case of regular lattice composites the parameter  $r_{ij}^0$  in eqn (42) can be replaced by the lattice constant  $r_p$ .

It should be noted that the current simulation model for the composite, besides having elastic properties discussed in this section, also maintains a bulk viscosity  $\nu$ . If the applied field is cyclic,  $E_z(t) = E_0 e^{i\omega t}$ , then the viscosity  $\nu$  of the composite can be defined from the rate of the composite response along the applied field,  $\nu = P_z^u L_z / (dL_z/dt)$ .<sup>77–79</sup> Here  $P_z^u$  is a stress created by the electrostatic forces  $F_{ji}$  defined in eqn (19). Because the forces  $F_{ji}$  are induced by the field  $E_z(t)$ , the viscosity  $\nu$  also depends on  $E_z(t)$ . For the calculation of  $\nu(E_z)$  a different set-up with a free surface is needed in order to measure  $dL_z/dt$  directly from the displacement of the boundary layer. Then, depending on the value of  $\omega\tau_c$ , where the composite relaxation time  $\tau_c$  and the bulk viscosity  $\nu$  is connected through the Debye–Stokes–Einstein relationship,<sup>80</sup> it is possible to estimate the energy dissipation and actuation hysteresis effects in the composite. For a zero field  $E_z = 0$ , the deformation rate  $dL_z/dt$  of the composite can be evaluated by applying an external mechanical perturbation  $P_z$  directly to the composite boundary (or to the opposite boundaries of the slab polymer). In the current set-up we are interested only in the response  $\Sigma_z$  of the bulk composite to static loads  $P_z(E_z)$  for  $E_z = \text{const}$ , therefore the issue of viscosity is out of scope of current consideration.

## 4 Simulation details

The calculation of the composite actuation relies on the resolving of the field-induced pressure components from the elastic deformations of springs and from the dipolar interactions between the inclusions. The pressure components can be directly determined from the corresponding force virials. For the latter the best suited method is Molecular Dynamics simulation. We used *NVT* ensemble Molecular dynamics simulations with a Verlet algorithm and a Nose thermostat to access the actuation strain of the composite with polarizable inclusions.  $N$  nanosized particles of diameter  $\sigma = 200$  nm at the volume fraction  $\eta = 0.0083$  were distributed in the bulk of the host

elastomer matrix. For the case of regular lattice composites, the lattice constants of the particle distributions are  $r_p = (\gamma V_p/\eta)^{1/3}$ , where the parameter  $\gamma$  takes values 1, 2, and 4 for the SC, BCC, and FCC composites correspondingly. For the case of random (homogeneous) particle distribution, the nearest-neighbor length scale is defined as  $r_p = 0.554(V_p/\eta)^{1/3}$  according to ref. 81. Each inclusion is attached by springs with spring constants  $\chi$  to its  $n_b$  nearest neighbors. For the SC composite  $n_b = 14$  and includes 6 nearest neighbors from the first coordination shell of radius  $r_p$ , and 8 neighbors from the second coordination shell of radius  $r_p\sqrt{2}$ . In the BCC composite each particle is connected to its 8 neighbors from the first coordination shell of radius  $r_p\sqrt{3}/2$ , and 6 neighbors from the second coordination shell of radius  $r_p$ , thus making the total  $n_b = 14$  again. For the FCC composite we used  $n_b = 12$  nearest neighbors in the first coordination shell of radius  $r_p\sqrt{2}$ . Schematically the spring-bead model for these composites is shown in Fig. 3, where blue-colored springs attach the chosen bead (colored blue) to its neighbours in the first coordination shell, and pink-colored springs attach it to its neighbours in the second coordination shell.

Finally, for the random distribution we chose the first nearest  $n_b = 14$  neighbors for each inclusion. A 3D view of the simulation setup for the case of BCC composite with  $N = 1024$  particles is shown in Fig. 4a.

Nearly all experimental studies<sup>33–42</sup> were done for high  $k$  inclusions randomly distributed in electrostrictive polymers, for which an enhancement of the contracting deformation is observed at fields up to  $20 \text{ MV m}^{-1}$ . In our current model we omit the electrostriction of the host matrix, assuming that it has a non-polar molecular structure. In other words, for a pure host matrix, assuming that the inclusions are part of the host polymer, putting  $\epsilon_p = \epsilon_m$  in eqn (10) and (11) will result in  $\mu_i = 0$  and  $F_{ij} = 0$ . The actuated performance of the pure polymer is defined by the Maxwell strain  $\Sigma_M$  in eqn (26). Our aim is to investigate composite deformations generated by the electrostriction effect of the dipolar inclusions. To get larger strains we apply stronger fields,  $250 \text{ MV m}^{-1}$  rather than the  $20 \text{ MV m}^{-1}$  in experiments, and consider a more elastic host polymer, the Young's modulus  $0.1 \text{ MPa}$  as compared to  $0.5\text{--}3000 \text{ MPa}$  in experiments. Because our own experiments with similar simulated composite parameters are in the preparation stage,

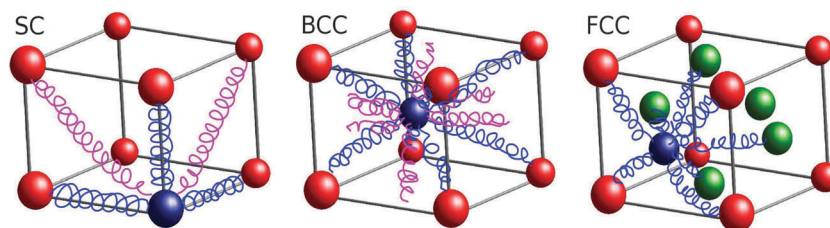


**Fig. 3** Schematic drawing showing details of the spring-bead model used for the SC, BCC, and FCC composite structures. Blue-colored springs attach the chosen blue-colored bead to its neighbours in the first coordination shell, and pink-colored springs attach it to its neighbours in the second coordination shell. Note that for the SC composite in the left picture and for the FCC composite in the right picture only the attachment to the neighbours belonging to the single cell are shown. For the BCC composite in the central picture the pink springs to the second coordination shell particles are shown partially in the single cell. The green spheres in the FCC composite represent the inclusions in the middle points of the cell faces.

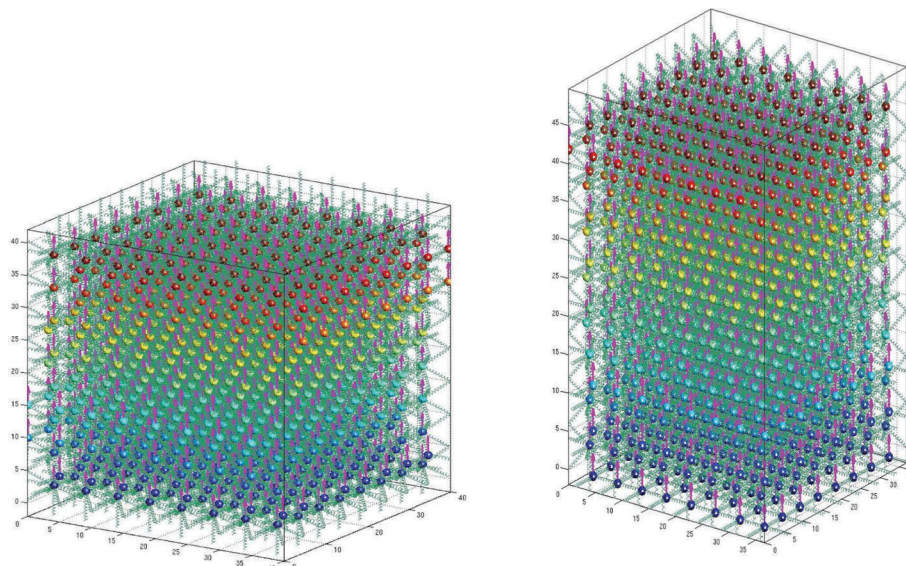


Fig. 4 Snapshots of the bead-spring model used for the BCC composite under the applied field  $E = 250 \text{ MV m}^{-1}$ . Left picture – the initial configuration at the simulation time  $t = 380 \text{ ps}$ , right picture – the final configuration at the simulation time  $t = 100 \mu\text{s}$ . Pink arrows represent the dipole moments of inclusions. Different bead colors correspond to the altitudes of the beads from the bottom plate  $x = 0$ . Springs are colored in green.

it is not yet possible to compare our simulation results with the experimental data.

The amplitude of the applied field  $E$  has an upper limit because of the clamping instability in dipolar systems at high fields. The value of the critical field  $E_c$  is analyzed in Appendix A.

The evolution of the stress-free initial system with  $E = 0$  to a new state with balanced electrostatic and elastic forces was controlled by the equivalence of the pressure components in all three directions. The pressure was calculated using the force virials

$$P = \frac{1}{3V} \sum_{j>i}^N \vec{r}_{ji} \cdot \vec{\Xi}_{ji} = P_x + P_y + P_z \quad (43)$$

where the forces  $\vec{\Xi}_{ij}$  between the particles  $i$  and  $j$  (the force acts on the particle  $i$  from the particle  $j$ ) include both the electrostatic forces  $\vec{F}_{ji}$  given by eqn (19) and the elastic forces

$$\vec{F}_{ji}^{\text{elastic}} = \chi(r_p - r_{ij}) \frac{\vec{r}_{ji}}{r_{ji}} \quad (44)$$

Here  $\vec{r}_{ji} = \vec{r}_i - \vec{r}_j$ , and for the elastic forces the summation in eqn (43) goes over the  $n_b$  neighbors of the inclusion  $i$ . The pressure components in eqn (43) are defined as

$$P_k = \frac{1}{3V} \sum_{j>i} \vec{k}_{ji} \cdot \vec{\Xi}_{ji}^{(k)} \quad (45)$$

for  $k = x, y, z$ . The equivalence of the pressure components  $P_k$  implies  $P_x = P_y = P_z$ , or

$$P_z = P_{xy} = \frac{P_x + P_y}{2} \quad (46)$$

During simulations this equivalency condition was implemented according to the protocol given in Appendix B.

## 5 Simulation results

All simulations were carried out using a time step  $h = 380 \text{ ps}$  and an equilibration time  $\Delta\tau = 380 \text{ ns}$ . The time for gathering the statistics was  $\Delta t = 38 \text{ ns}$ . The following parameters for the host matrix and inclusions were considered:  $\epsilon_p = 100$ ,  $\epsilon_m = 2$ ,  $Y = 0.1 \text{ MPa}$ , and  $\eta = 0.083$ . Putting these values into eqn (30) and (31) we get for the composite  $\tilde{\epsilon}_m = 2.06$  and  $\tilde{Y} = 0.103 \text{ MPa}$ . Then, according to eqn (26) the Maxwell strain will be

$$\Sigma_M = 4.42 \times 10^{-17} (\text{mV}^{-1})^2 \cdot E^2 \quad (47)$$

where  $E$  is the amplitude of the applied field given in  $[\text{V m}^{-1}]$  units. Whereas our setup does not explicitly include the Maxwell pressure acting on the surface of the whole composite membrane, we assume that the strain calculated for the simulation box will be the same for the whole membrane, and therefore, its strength should be compared with the Maxwell strain.

The lattice constants  $r_p$  for the regular particle distributions are: SC-4 $\sigma$ , BCC-5 $\sigma$ , and FCC-6.3 $\sigma$ . The critical field  $E_c$ , defined in Appendix A, for the system setup from eqn (60) is about  $E_c \approx 500 \text{ MV m}^{-1}$ . We used twice weaker fields  $E = 250 \text{ MV m}^{-1}$  for the maximal applied field.

In Fig. 5 we show the evolution of the pressure components  $P_z$  and  $P_{xy}$  during the simulation time for the FCC composite at  $E = 200 \text{ MV m}^{-1}$ . At the initial time  $t = 0$ , when a stress-free composite is put under external field  $E$ , the dipole-dipole interaction between the inclusions attempts to elongate the composite along the  $z$ -axis direction making  $P_z > P_{xy}$ . For balancing these two components, the system size is increased along the  $z$  direction with simultaneous decreasing of its lateral dimensions. This leads to the drop of the pressure component  $P_z$  and to the rise of the pressure component  $P_{xy}$ . When the two pressure components reach the same value, the composite enters into a stable

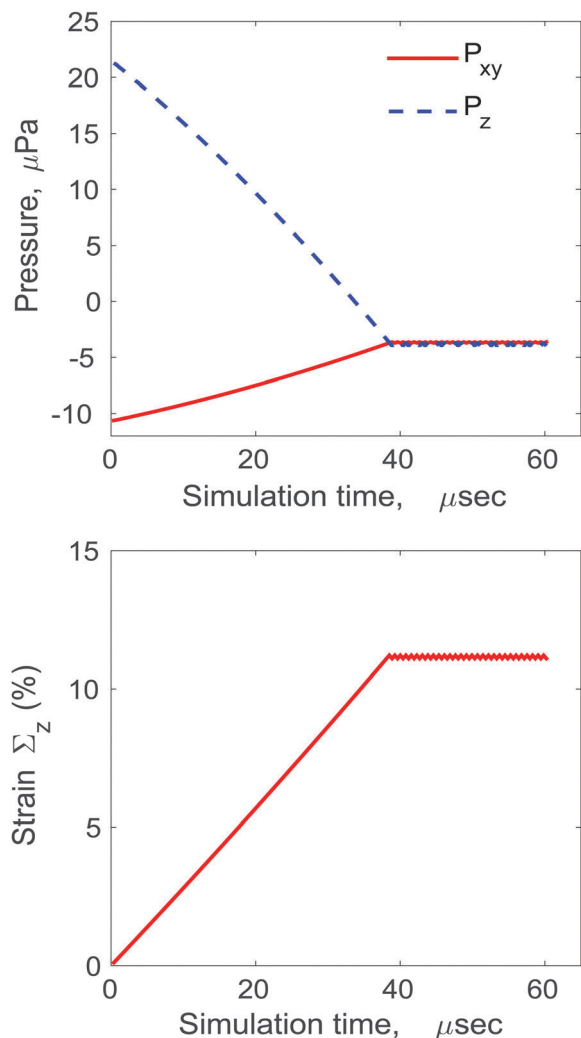


Fig. 5 Upper figure: the  $P_{xy}$  and  $P_z$  components of the total pressure calculated from the virials of the electrostatic (eqn (19)) and elastic (eqn (44)) forces, as a function of the simulation time. Red solid line is for  $P_{xy}$ , and dashed blue line is for  $P_z$ . Bottom figure: The evolution of the composite strain. Other system parameters are:  $E = 200 \text{ MV m}^{-1}$ , a FCC composite,  $\eta = 0.0083$ .

polarized state. The time resolved evolution of the composite strain is shown in Fig. 5. Following the drop of the pressure component  $P_z$  the strain linearly increases and reaches its equilibrium value  $\Sigma_z = 12\%$  at which the difference between the pressure components becomes zero. The small fluctuations of the strain  $\Sigma_z$  around its equilibrium value are related to the amplitude of the size increment  $\delta$  of the simulation box size  $L_z$ . Even at the equilibrium state, the balance between the pressure components in the composite is tested by random attempts to change the composite thickness by  $\delta$ . Decreasing the value of  $\delta$  will decrease the amplitude of fluctuations in  $\Sigma_z$ , however it will increase the simulation time needed for the composite to reach the equilibrium state.

### 5.1 Actuation of the SC, BCC, FCC, and random composites

Calculated strains for composites with different particle distributions as a function of the applied field  $E$  are collected in Fig. 6.

Negative strains in this figure mean a contraction, and positive strain means an elongation of the composite. The homogeneous (random) distribution of inclusions provides the strongest contraction with  $\Sigma_z$  reaching almost  $-50\%$  at  $E = 250 \text{ MV m}^{-1}$ . The SC distributed inclusions also generate sufficiently strong negative strain. At the same time other regular lattice composites reveal an elongation, with the BCC composite having a stronger response than the FCC composite. Note that in the regular lattice composites with non-zero strains the following transitions take place: SC to a simple tetragonal lattice, BCC to a body-centered tetragonal (BCT) lattice, and FCC to face-centered tetragonal (FCT).

The contraction of the random composite can be understood using the following analytical approach. Let us assume that an inclusion  $i$  is wrapped by a fictitious shell of radius  $r_p$  and thickness  $\delta r$ . There are  $N_s = 4\pi r_p^2 \delta r \rho_p$  dipoles homogeneously distributed in this shell. The force between the central dipole  $i$  and the dipole  $j$  from the shell, which is given by eqn (19), can be rewritten as

$$\vec{F}_{ji}(r) = \frac{1}{4\pi\epsilon_0\epsilon_m} \frac{3\mu^2}{r_{ji}^4} \left[ (1 - 5\cos^2\theta)\vec{e}_{r_{ji}} + 2\cos\theta\vec{e}_{\vec{\mu}} \right] \quad (48)$$

for the case of aligned dipoles  $\vec{\mu}_i \parallel \vec{\mu}_j \parallel \vec{z}$ . Here  $\theta$  is the angle between the  $\vec{r}_{ji}$  (directed from  $j$  to  $i$ ) and the axis  $\vec{z}$ ,  $\mu$  is the amplitude of  $\vec{\mu}_i = \vec{\mu}_j$ , and  $\vec{e}_{r_{ji}}$  and  $\vec{e}_{\vec{\mu}}$  are unit vectors along the separation distance and dipole moments correspondingly. We calculate spherically averaged force components  $\vec{F}_{ji}\vec{e}_z$

$$\langle \vec{F}_{ji}\vec{e}_z \rangle_\theta = A \left[ \int_0^{\pi/2} (1 - 5\cos^2\theta)\cos\theta + 2\cos\theta\cos\theta \right] \rho(\theta)\sin\theta d\theta \quad (49)$$

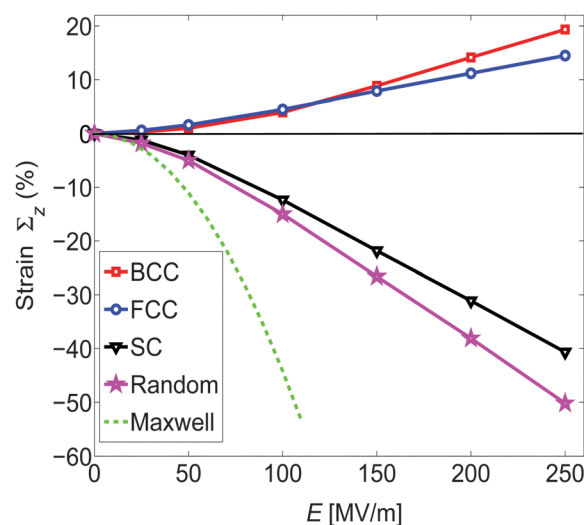


Fig. 6 Deformation of the composite under the applied field  $E$  oriented in the  $[001]$  direction for parameters  $Y = 0.1 \text{ MPa}$ ,  $\epsilon_p = 100$ ,  $\epsilon_m = 2$ . Four different spatial distributions for the inclusions are used: BCC – red line with squares, FCC – blue line with circles, SC – black line with triangles, and random distribution – pink line with stars. Whereas the BCC and FCC composites elongate, the SC and random composites contract. Green dashed line represents the Maxwell strain  $\Sigma_M$  given by eqn (47).

and  $\vec{F}_{ji}\vec{e}_{xy}$ ,

$$\langle \vec{F}_{ji}\vec{e}_{xy} \rangle_{\theta} = -A \int_0^{\pi/2} (1 - 5 \cos^2 \theta) \sin \theta \rho(\theta) \sin \theta d\theta \quad (50)$$

in the upper hemisphere  $0 < \theta < \pi/2$ . Here  $\vec{e}_z$  is a unit vector along the  $z$ -axis, and  $\vec{e}_{xy}$  is a unit vector perpendicular to the applied field and directed from the central dipole  $i$  outwards to the shell particles. Note that the averaging over  $0 < \theta < \pi$  in eqn (49) and (50) might lead to the mutual cancellation of the force components in the upper and bottom hemispheres. The function  $\rho(\theta)$  in eqn (49) and (50) is the angular dependence of the dipole distribution, and the prefactor  $A = \frac{3}{2} \frac{\mu^2}{\epsilon_0 \epsilon_m} \bar{r}_{ji}^4$

has no  $\theta$  dependence. By putting  $\rho(\theta) = 1$  for the uniform distribution of dipoles valid for the random composite, we have

$$\langle \vec{F}_{ji}\vec{e}_z \rangle_{\theta} = A \left[ -\frac{1}{2} \cos^2 \theta + \frac{5}{4} \cos^4 \theta \right]_0^{\pi/2} = -\frac{3}{4} \quad (51)$$

$$\langle \vec{F}_{ji}\vec{e}_{xy} \rangle_{\theta} = -A \left[ -\frac{\theta}{8} - \frac{\sin(2\theta)}{4} + \frac{5}{32} \sin(4\theta) \right]_0^{\pi/2} = \frac{\pi}{16} \quad (52)$$

The negativity of  $\langle \vec{F}_{ji}\vec{e}_z \rangle_{\theta}$  means shell contraction along the  $z$ -axis. A positive value of  $\langle \vec{F}_{ji}\vec{e}_{xy} \rangle_{\theta}$  corresponds to the repulsion of the shell particles from the central dipole  $i$  in the lateral direction. Thus, a combined result of these two terms is a net contraction of the random composite along the applied field  $E$ . This pure dipolar argument defines the electrostriction effect in the random composite. For finding the total composite actuation the contribution from elastic springs should also be calculated.

Using similar arguments it is possible to comprehend the contraction of the SC composite. In this case the angular averaging in eqn (49) and (50) should be done over angles  $\phi$  and  $\theta$ , and the dipolar distribution in the shell  $\rho(\phi, \theta)$  a sum of the Dirac functions  $\rho(\theta, \phi) = \delta(\theta)\delta(\phi) + \sum_{i=0}^3 \delta\left(\theta - \frac{\pi}{2}\right)\delta\left(\phi - \frac{\pi}{2}\right)$  should be used. However, the simplest way to evaluate the composite actuation is to use the expression for the interaction between a pair of parallel dipolar chains per particle<sup>65</sup> (we show here the leading term of the interaction)

$$U_{cc}(r, z) = \frac{2\pi\mu^2}{\epsilon_0\epsilon_m r_p^3} \sqrt{\frac{r_p}{r}} e^{-\frac{2\pi r}{r_p}} \cos \frac{2\pi z}{r_p} \quad (53)$$

Here  $r$  is the chain-chain separation distance,  $z$  is the vertical shifting parameter, and the energy is scaled per particle. In the SC composite with its [001] orientation being parallel to the applied field, each chain of dipoles has four nearest chains of the same orientation with  $r = r_p$  and  $z = 0$ . For this case the interaction potential  $U_{cc} > 0$  and the neighboring chains are repelled from the central chain. Such lateral repulsion in the SC composite results in its contraction in the  $\vec{z}$  direction.

For the BCC and FCC composites, each dipolar chain is also surrounded with its four nearest chains at separation distances  $r = r_p/\sqrt{2}$  and  $r = r_p/2$  correspondingly, with  $z = r_p/2$  for both

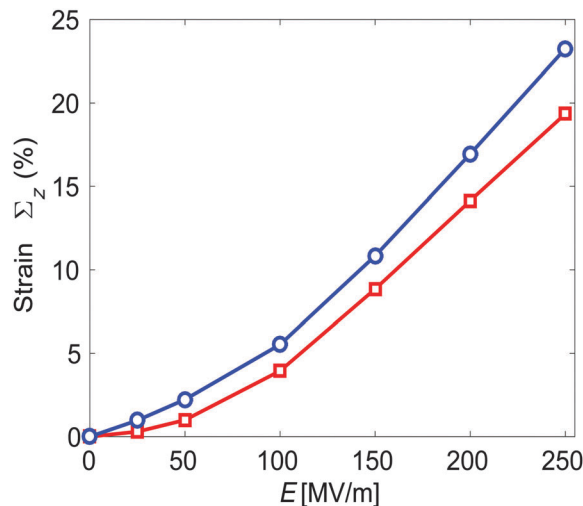


Fig. 7 Deformation of the BCC composite under the applied field  $E$ . Other system parameters are:  $Y = 0.1$  MPa,  $\epsilon_p = 100$ ,  $\epsilon = 2$ ,  $\eta = 0.0083$  (red line with squares) and  $\eta = 0.064$  (blue line with circles).

composites. Putting these values into eqn (53) we get  $U_{cc} < 0$  for the BCC and FCC composites. Such lateral attraction in the composite is equivalent to the elongation in the longitudinal direction.

In Fig. 6 we also show the contribution from the Maxwell strain in eqn (26). This strain appears to be more than twice stronger than the electrostrictive strain of the composites for the current system parameters. As it has been discussed in Section 2.3, at large strains the linear approximation should be replaced by the modified theory given in ref. 16 which predicts smaller strain values. Therefore, the Maxwell data at the applied field  $E > 50$  MV m<sup>-1</sup> overestimates the true strain of the material. At the same time, at low fields  $E < 50$  MV m<sup>-1</sup>, the Maxwell data can be assumed reliable. It is stronger than other strains in that area. Obviously, for larger inclusions with a higher dielectric constant, which will result in a much stronger dipolar interaction between the inclusions, the positive strain of the BCC and FCC composites will be stronger than the Maxwell strain. The latter very weakly depends on the size and dielectric constant of particles, mainly through the mixing rules eqn (30) and (31). Note also that for  $\epsilon_m = 2$  considered for the host matrix, the Maxwell strain for the constant voltage condition given by eqn (28) coincides with the strain shown in Fig. 6.

The effect of the inclusion packing fraction  $\eta$  on the composite actuation is analyzed in Fig. 7 on the example of the BCC composite. The increase of  $\eta$  enhances the composite actuation because of the stronger dipole-dipole interaction at smaller separation distances. However, it should be noted that at high  $\eta$  the effective composite elasticity constant  $\tilde{Y}$  given by eqn (31) might become big enough resulting in a weakened composite actuation.

## 5.2 Lattice randomness effects on the composite actuation

We now investigate how the deviation of the inclusion position from the true lattice sites might alter the composite actuation.

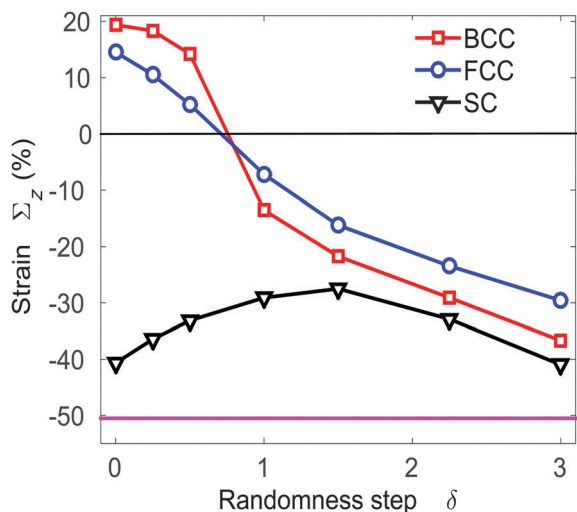


Fig. 8 Dependence of the composite strain  $\Sigma_z$  on the randomness parameter  $\delta$  for the SC, BCC, and FCC composites. Other parameters are:  $E = 250 \text{ MV m}^{-1}$ ,  $Y = 0.1 \text{ MPa}$ ,  $\varepsilon_p = 100$ ,  $\varepsilon_m = 2$ , and  $\eta = 0.0083$ .

Such spatial distribution defects always exist in experimental studies. The imperfectness of the spatial distribution of inclusions  $\{\vec{r}_{ij}\}$  can be estimated by the randomness parameter

$$\delta = \frac{1}{N\sigma} \sum_j^N |\vec{r}_{ij} - \vec{r}_0| \quad (54)$$

where  $\vec{r}_0$  denotes the positions of the lattice sites. For each randomness parameter  $\delta$  we generate a sphere of radius  $\delta$  around each lattice site and assign a random point from its surface to the inclusion position. Simulation results for the actuation of the SC, BCC, and FCC composites are shown in Fig. 8. We see that, as the parameter  $\delta$  increases, the strength of elongation of the BCC and FCC composites gradually fades away and at about  $\delta \approx 0.8$  reverses to a complete contraction.

The behavior of the SC composite in Fig. 8 stands separate from the monotonic behavior of the BCC and FCC composites. The contraction of the SC composites first weakens by going up to smaller  $-\Sigma_z$  values, and then enhances going back to the higher  $-\Sigma_z$ . Such nonlinear behavior is a consequence of the fact that in the SC composite the dipolar chains have maximal mutual repulsion because of the zero shifting along their  $\vec{z}$  positions. Therefore, any non-zero shifting  $z$  brought by the randomness parameter  $\delta$  into the chain positions will definitely decrease the chain-chain repulsion in eqn (53), or equivalently, weaken the composite contraction. For larger  $\delta$  the simulated systems behave like a random composite, and thus the actuation of all regular lattice composites approaches the random composite strain value of about 50% (see the pink line in Fig. 8).

### 5.3 Actuation of distorted lattice composites

We now examine how the initial distortion of the lattice structure of the inclusion distribution alters the composite actuation. For this purpose we fix the packing fraction of inclusions to  $\eta = 0.0083$ , and change the ratio of the lattice constants  $\ell = c/a$ , where  $c$  is the lattice constant of the regular

lattice in the  $\vec{z}$  axis direction, and  $a$  is the lattice constant in the  $x$  and  $y$  directions. In all cases we limit ourselves to the consideration of symmetric distortions of the initial structure in the  $xy$  plane. In other words, instead of starting with SC, or BCC, or FCC lattice composites with  $\ell = 1$ , we chose different simple tetragonal, BCT and FCT lattice composites with  $0.4 < \ell < 2.5$  as the starting configuration for the composite.

The calculated electrostatic energies  $V_{ij}$  per particle, given by eqn (21), for the distorted SC, BCC, and FCC composites are plotted in Fig. 9 for an applied field of  $E = 1 \text{ MV m}^{-1}$ . At low distortion ratio  $\ell$  of the initial structure, which corresponds to a configuration of dipolar chains separated by a distance larger than the separation between the intra-chain dipoles, the main contribution to the electrostatic energy comes from the intra-chain dipole-dipole attractions. That is why all the energy curves in Fig. 9 have negative values at low  $\ell$ . At high  $\ell$  values, which correspond to the configuration of dipolar sheets (2D plates) separated by a distance larger than the inter-sheet separation between the dipoles, the main contribution to the electrostatic energy stems from the intra-sheet dipole-dipole repulsion. This is seen as the upward increase of energy curves in Fig. 9 at large  $\ell$ . Between these two extreme cases for  $\ell$  the electrostatic energy for the BCC and FCC composites has nonmonotonic dependence on  $\ell$ . The energy curve for the BCC composite has a maximum at  $\ell_{\max} = 0.7664$  and a minimum at  $\ell_{\min} = 1.6565$ . For the FCC composite these values are  $\ell_{\max} = 0.5637$  and  $\ell_{\min} = 1.241$  correspondingly. The position of  $\ell_{\max}$  corresponds to a metastable state, and any small deviation, either elongation or contraction of the initial system, from this position will be energetically favorable. An opposite behavior is expected for the system with a distortion ratio of the initial structure  $\ell_{\min}$ . In this case the composite stays forever at this position, because all other states in its vicinity are unfavorable and thus will try to elongate, or contract,

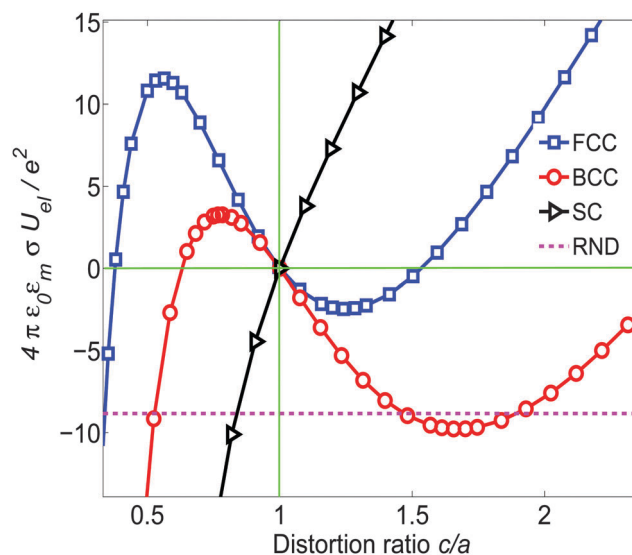


Fig. 9 The calculated total electrostatic energy per particle  $U_{el} = \frac{1}{N} \sum_{ij=1}^N V_{ij}$  for the distorted SC, BCC, and FCC composites with  $\eta = 0.0083$  as a function of the distortion ratio of the initial structure  $\ell = c/a$ . Applied field is  $E = 1 \text{ MV m}^{-1}$ .

depending on which side of  $\ell_{\min}$  they are standing, for reaching the  $\ell_{\min}$  state.

To further analyze the meaning of  $\ell_{\max}$  and  $\ell_{\min}$  in Fig. 9, we compare their values with the stability points of hard sphere dipolar systems and electrorheological fluids.<sup>63–65,82–84</sup> For systems with permanent dipoles, it is known that as the dipole moment of spheres increases, the ground state of the system changes from the apolar BCC lattice structure to a polarized BCT lattice structure. The lowest energy for the BCT structure

happens at the size ratio  $\frac{c}{a} = \sqrt{\frac{2}{3}} = 0.817$ , with  $c = \sigma$  corresponding to the case of touching dipoles along the  $\vec{z}$  axis. The [110] plane of this BCT has a triangular lattice with the lattice constant  $c$ , and the cell is polarized in the perpendicular to this plane direction. A similar BCC–BCT behavior is also observed in electrorheological colloidal suspensions.<sup>65,83,85</sup> Here the BCT structure is also composed of touching dipoles along  $z$  direction with  $c = \sigma$ , and the size ratio is  $c/a = 0.817$ . This value is larger than our result  $\ell_{\max} = c/a = 0.7664$  because of the following reasons. First, the implemented constant cell volume condition  $r_p^3 = ca^2$  implies that for the BCT with  $c = \sigma$

the size ratio is  $\ell = \left(\frac{\sigma}{r_p}\right)^{\frac{3}{2}}$  and depends on the initial lattice constant  $r_p$ . For  $r_p = 5\sigma$  used for the BCC composite, the size ratio for which a stable BCT with touching dipoles exists is  $\ell = 0.09$ . This value is much smaller the value  $\ell = 0.817$  which corresponds to the BCT deformation of the BCC lattice with  $r_p = 1.1547\sigma$ . Second, whereas the BCT of hard sphere dipolar system and electrorheological colloids is stable at  $\ell = 0.817$ , our BCT with  $\ell = 0.7664$  is unstable as discussed above.

A detailed analysis of the curves shown in Fig. 9 reveals several other interesting observations:

- (i) for a given distortion ratio of the initial structure  $\ell = c/a$  the BCC structure is always more stable than the FCC structure.
- (ii) the random distribution of inclusions is not always the structure with minimal energy per particle. The polarized BCC phase is more favorable in the region  $1.5 < \ell < 2$ , and the SC composite is favorable for  $\ell < 0.85$ .
- (iii) all regular lattice structures have very small negative values at  $\ell = 1$ . The rescaled energy per particle  $U_{\text{el}}(\ell) =$

$4\pi\epsilon_0\epsilon_m\sigma N^{-1} \sum_{ij=1}^N V_{ij}(\ell)/e^2$  is  $-3.16 \times 10^{-3}$  for the FCC lattice,  $-1.52 \times 10^{-2}$  for the BCC lattices, and  $-3.05 \times 10^{-2}$  for the SC lattice.

It is evident that electrostatic energy curves are useful for predicting the response of the composite to external fields. We introduce the so-called Polarization Driven strain  $\Sigma_{\text{PD}}$ , defined as the derivative of the electrostatic energy over the distortion ratio of the initial structure,

$$\Sigma_{\text{PD}} = -\frac{dU_{\text{el}}(\ell)}{d\ell} \quad (55)$$

This quantity is plotted in Fig. 10, together with the calculated strain of the distorted structures.

There is a good qualitative agreement between the simulated  $\Sigma_z$  and polarization-driven  $\Sigma_{\text{PD}}$  strains for the regular lattice composites. For the BCC and FCC composites both strains,  $\Sigma_z$  and  $\Sigma_{\text{PD}}$ , have a window of elongation and both strains cross the zero-strain line at the same distortion points. These crossing points correspond to the extremes of the electrostatic potential shown in Fig. 9, and thus have different natures. The crossing points on the left of the maximum in Fig. 10a and b are metastable points, and the crossing point at the right side of the maximum  $\Sigma_z$  is the stability point. The nature of the crossing points can also be recognized from the slope of lines tangent to the strain curves at these points. A steeper slope usually indicates metastability of the corresponding point.

The strain results reported in ref. 28 for the distorted BCC composite only covers the metastable area around  $\ell_{\max}$  where a negative-to-positive strain transition is observed similar to our finding. In that sense our results cover a wider range of the distortion ratio of the initial structure and predict the existence of the second crossing point. The position of the maximum of  $\Sigma_z$  for the BCC composites is around  $\ell_{\text{BCC}} \approx 1$ , and for the FCC composite it is around  $\ell_{\text{FCC}} \approx 0.75$ . The ratio of these two positions,  $\ell_{\text{FCC}}/\ell_{\text{BCC}} \approx 1/\sqrt{2}$  corresponds to the martensitic transition FCC–BCC, when the shrinking of FCC lattice along its [001] direction  $\sqrt{2}$  times transfers it to a BCC lattice.

The SC composite experiences a contraction for all distortion ratios  $\ell$  of the initial structure. However, there is a noticeable local maximum at  $\ell \approx 1.4$ . We believe that the non-monotonicity of the strain stems from two different contributions to the electrostatic energy: the intra-chain attraction along the  $\vec{z}$  axis, and the chain–chain repulsion in the lateral direction. These contributions have different dependence on the distortion ratio of the initial structures  $\ell$ : the intra-chain attraction decreases as  $1/\ell^3$ , whereas the chain–chain repulsion decreases as  $\sqrt{\ell}$  at large  $\ell$ .

## 6 Guidelines for experimental realization of theoretical predictions for the composite actuation

We anticipate that the realization of ordered inclusion distributions is not an easy task in experimental studies. For achieving ordered lattice structures or uniform particle distributions in experiments, the concept of polymer-grafted nanoparticles can be implemented.<sup>5</sup> The nanoparticles can be also charged to facilitate their aggregation into ordered morphologies at elevated temperatures before freezing their positions at room temperature.

The chosen dielectric permittivity and elasticity parameters for the host matrix are close to the corresponding parameters of the Very High Bond acrylic elastomer (3 M VHB), which has  $\epsilon_m = 4.7$ ,  $Y = 0.5$  MPa, and of the styrene–(ethylene-co-butylene)–styrene triblock copolymer (SEBS), which has  $\epsilon_m = 2$ ,  $Y = 1$  MPa. Smaller  $Y$  in simulations provides larger actuation strains and thus a better resolution between different types of composite

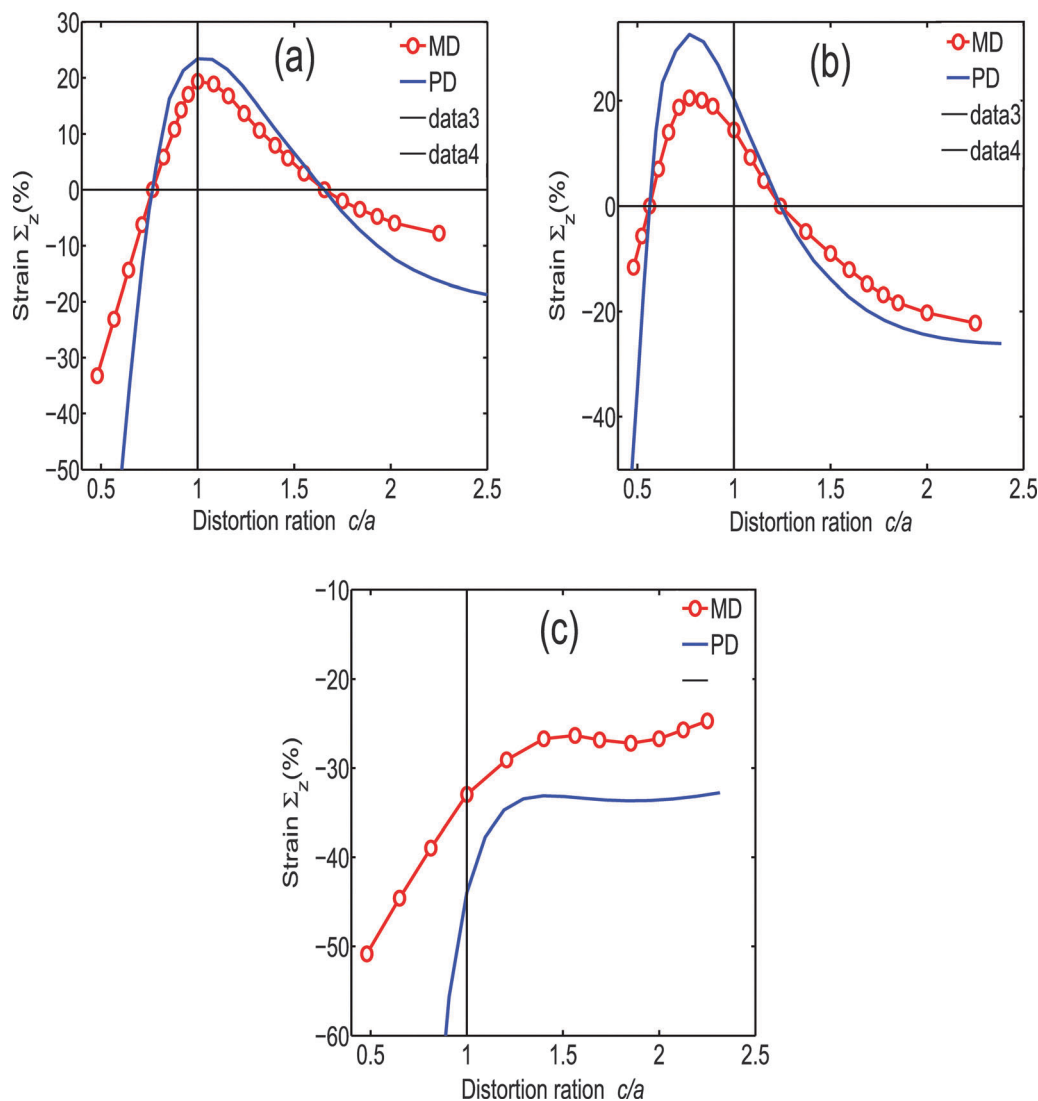


**Fig. 10** Deformation of the BCC (a), FCC (b), and SC (c) composites as a function of the distortion ratio  $\ell = c/a$  of the initial structure. Line with symbols: simulation results, full line: the prediction of the Polarization Driven strain in eqn (55). Other parameters are:  $E = 250 \text{ MV m}^{-1}$ ,  $Y = 0.1 \text{ MPa}$ ,  $\varepsilon_p = 100$ ,  $\varepsilon = 2$ ,  $\eta = 0.0083$ . (a) BCC, (b) FCC, (c) SC.

actuators. Whereas the molecular weight and the internal structure of the polymer are not directly accounted for in our simulation model, the following two assumptions are made on them: (i) the polymer molecule has no molecular dipoles, and (ii) the molecules form a mesh network with homogeneous structure in all directions. The first assumption guarantees that the applied fields does not infer any structural changes to the polymer molecules and thus no internal electrostriction effect takes place. The second assumption is necessary for using the same spring-constant  $\chi$  for all connecting springs in our spring-bead model.

According to our simulation results, a better choice for the host matrix is an elastomer with low Young's modulus  $Y$ . The choice for  $\varepsilon_m$  and for the dielectric contrast parameter  $\varepsilon_p/\varepsilon_m$  depends on the actuation purpose of the composite. If the composite is intended to have enhanced Maxwell-type contractions, then both  $\varepsilon_m$  and  $\varepsilon_p/\varepsilon_m$  should be large, and the particles

have to be randomly distributed, or to follow the SC spatial distribution. In the opposite case, if the composite is designed for having large elongations along the field, then  $\varepsilon_m$  should be small for getting low Maxwell stress values, whereas the contrast parameter  $\varepsilon_p/\varepsilon_m$  should be large. Additionally, for this case the spatial distribution of particles should strictly follow either the BCC or the FCC structures. For further optimization of the composite parameters, current research should be expanded to elaborate the role of the particle size  $R$  and its volume fraction  $\eta$ .

## 7 Concluding remarks

We have shown that the electrostriction effect, which is a significant contribution to the actuation of low aspect-ratio composites, strongly depends on the spatial distribution of

inclusions. Whereas the composites with homogeneously (randomly) distributed inclusions always contract along the applied field, the actuation of regular lattice composites depends on their lattice structure: the SC composite always shrinks, but the BCC and FCC composites show a net elongation response along the applied field oriented parallel to the [001] direction of the lattice.

The elongation of the BCC and FCC composites was additionally examined against the defects in the lattice structure of the spatial distribution of inclusions. We show that at large defects, measured by the randomness parameter, the elongation of the BCC and FCC diminishes and switches to a net contraction. Similar effects are observed for initially distorted lattices with the distortion ratio parameter  $\ell \neq 1$ . Here we detect the existence of an elongation window, inside which the BCC and FCC composites experience an elongation, and beyond which the composites contract. It should be noted that the elongation window reported by Zubarev *et al.*<sup>30,31</sup> and Morozov *et al.*<sup>32</sup> are different from our findings. Both groups explicitly considered the dependence of the macroscopic electrostatic effect on the shape aspect ratio, whereas we detect the elongation window considering only the electrostriction effect as a function of the distortion ratio of the initial structure.

We finally comment on the possible extension of the research reported here. First, the monodisperse dipolar system considered here can be extended to a more realistic polydisperse dipolar system. In this case, a specific treatment of the bonding springs between the particles should be taken for two following reasons: (i) larger/smaller particles have larger/smaller surfaces and thus the elastic forces from the polymer matrix should be properly graded to account for this problem. (ii) The ground states of the polydisperse system under an applied field will depend on the polydispersity parameter.

Second, the macroscopic polarization theory used in this paper corresponds to the far field solution of the Poisson's equation of polarization. At high volume fractions of the inclusions this approximation should be replaced by the near field solutions which contain higher order multipoles of the dipolar field.

Third, the strain elastic energy in Section 2.4 is calculated using the Gaussian chain statistics and Hookian springs applicable to low strain amplitudes  $|\Sigma_z| \leq 30\text{--}40\%$ . This statistics should be replaced by the Langevin chain statistics briefly discussed at the end of Section 2.4. Under the Langevin statistics, which corresponds to the FENE nonlinear springs between the inclusions, we expect that the actuation of the composite will be smaller than the reported here simulation results in the high strain regions.

Fourth, in the current study the vertical change  $\Delta L_z$  of the simulation box was coupled with the symmetrical changes in the lateral box dimensions  $\Delta L_x = \Delta L_y$ . As a result of this we observed the BCC to BCT and FCC to FCT transitions under applied fields. The other possible transitions are the BCC to BCO (body centered orthorhombic) and FCC to FCO (face centered orthorhombic) transitions for which the three box

dimensions should be changed separately.<sup>82</sup> In order to test the occurrence of stable BCO or FCO transitions we will accompany each shape-changing simulation step by the additional variation of the  $L_x/L_y$  ratio.

Fifth, in the current simulation model the pressure components were calculated for all nodes, and averaged over all inclusions. As a result, the change of the simulation box shape was implemented for all nodes at the same ratio. For the case of polydisperse inclusions this approach needs to be modified by allowing local shape changes inside the simulation box.

Sixth, the actuation of the composite can be further enhanced by replacing the high-dielectric inclusions with either charged multilayers,<sup>86</sup> or layered ferromagnetic elastomers<sup>72</sup> for the magnetic actuation purposes. Our recent works<sup>72,86</sup> showed that by varying the internal parameters of these materials, such as the number of layers, the dielectric and elastic constants and the thicknesses of the layers, the actuation of these layered materials can be effectively controlled. For example, for a charged multilayer elastomer we detected a window of elongation with  $\Sigma_z \approx 150\%$  for the interface charge density  $0.01 \text{ C m}^{-2}$ . Putting these layered elastomers into the host matrix can tremendously reinforce the composite actuation. Such a double-actuation concept has a potential to develop into a new field of the electroactive composite research.

## Appendix

### A Stability region for composite actuation

Composites with polarizable inclusions are supposed to sustain their original elastic properties during the repeated actuation cycles under the applied fields. In other words, elastic forces of the host polymer should restore the initial state of the composite when the load is removed. This is only possible if the amplitude of the applied field does not exceed a critical field  $E_c$  above which the dipolar attraction triggers a clamping of dipoles into a touching configuration. When such clamping happens, with no host matrix material between the touching dipoles, there will be no restoring force to separate the dipoles at lower fields. As a result, the composite will lose its actuation capability forever. In this appendix we analyze the properties of the clamping instability.

For the head-to-tail oriented dipoles we introduce a dimensionless stability parameter

$$\psi(r) = \left| \frac{E_{\text{elastic}}(r)}{V_{ij}(r)} \right| \quad (\text{A1})$$

which measures the balance between the dipole-dipole attraction potential  $V_{ij}(r)$  given by eqn (21), and the elastic energy of the host matrix deformation,

$$E_{\text{elastic}}(r) = \frac{1}{2}\chi(r_p - r)^2 = \frac{2\pi Y}{3}(r_p - r)^2 r_p \quad (\text{A2})$$

where  $\chi$  is given by eqn (42). Putting  $\theta = 0$  in eqn (21) for the stability parameter  $\psi$  we get

$$\psi\left(\frac{r}{\sigma}\right) = A\left(\frac{r_p}{\sigma} - \frac{r}{\sigma}\right)^2 \left(\frac{r}{\sigma}\right)^3 \quad (\text{A3})$$

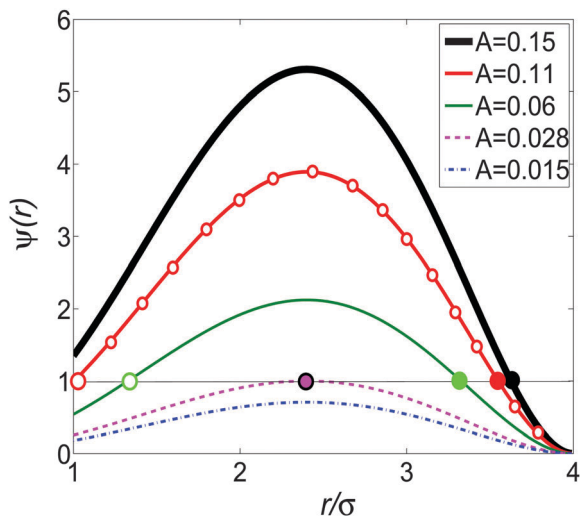


Fig. 11 The stability function  $\psi(r)$  from eqn (A3) against the separation distance between the dipoles for the nearest neighbor distance  $r_p = 4$  and different prefactors  $A$  given by eqn (A4). From bottom to top:  $A = 0.015$ ,  $0.028$ ,  $0.06$ ,  $0.11$ , and  $0.15$ . Critical field  $E_c$  in eqn (A5) is defined for the line  $A = 0.11$ .

where the distance independent coefficient  $A$  is

$$A = \left( \frac{\epsilon_p + 2\epsilon_m}{\epsilon_p - \epsilon_m} \right) \frac{2\epsilon_m Y r_p}{3\epsilon_0 E^2 \sigma} \quad (\text{A4})$$

Several representative curves for  $\psi(r)$  are plotted in Fig. 11. At small  $A = 0.015$ , see the thin dot-dashed (blue in color version) line,  $\psi(r) < 1$  for all separation distances  $\sigma < r < r_p$ . For this case the composite is completely vulnerable to the dipole clamping, *i.e.* when the field is switched on, the dipoles along the field will decrease their separation until a touching configuration  $r = \sigma$  is achieved. When the prefactor is  $A = 0.15$ , see the thick solid line (black in color version) in Fig. 11,  $\psi(r) > 1$  for all separation distances, meaning that the composite is completely robust against any clamping. In this case the dipoles along the field direction will decrease their separation from  $r_p$  to  $r_c$ , where  $r_c$  is the crossing point position shown as a filled black circle in Fig. 11. For intermediate values of  $A$ , we have a single-point stability state for  $A = 0.028$ , a partially stable state for  $A = 0.06$ , and a fully stable state for  $A = 0.11$ . For all these cases the composite actuation is defined by the distance between the point  $r_p = 4$  and the position of the right hand crossing point shown as filled circles in Fig. 11. The barrier between the latter and the left-hand crossing points, shown as open circles, keeps the composite safe from possible dipolar clampings. When the left crossing coincides with  $r = \sigma$ , which corresponds to the line  $A = 0.11$  in Fig. 11, the system becomes completely safe against any clampings. Thus the condition,  $\psi(r = \sigma) = 1$ , can be used to define the critical electric field,

$$E_c \approx \left( \frac{\epsilon_p + 2\epsilon_m}{\epsilon_p - \epsilon_m} \right) (r_p^* - 1) \sqrt{Y \epsilon_m r_p^*} \times 0.19 \text{ MV m}^{-1} \quad (\text{A5})$$

below which the actuation will be reversible. Here  $r_p^* = r_p/\sigma$ , and  $Y$  is given in  $\text{N m}^{-2}$  units. The typical values for  $E_c$  are discussed in the section of simulation results.

## B Simulation stages for the composite actuation

The equivalence of the pressure components in eqn (46) was implemented using the following consecutive simulation stages.

Stage (1) the system is equilibrated under the applied field  $\vec{E}$  during the simulation time  $t = \Delta\tau$ .

Stage (2) the statistics for the pressure components are gathered during the simulation time  $\Delta\tau < t < \Delta\tau + \Delta t$ , and at  $t = \Delta\tau + \Delta t$  the average pressure  $\bar{P}_i = \frac{1}{\Delta t} \sum P_i(t)$  for  $i = x, y, z$  is calculated.

Stage (3) the difference between the pressure components  $\bar{P}_z$  and  $\bar{P}_{xy}$  is calculated,  $\Delta P = \bar{P}_z - \bar{P}_{xy}$ .

Stage (4) at the simulation time  $\Delta\tau + \Delta t + h$  the cell size  $L_z$  is changed to  $L_z' = L_z + \delta$ , where the value of the size increment  $\delta$  is chosen to be a tiny fraction  $s$  of  $L_z^0$ ,  $s \ll 1$ , and the sign of  $\delta$  is defined according to the relation  $\delta = sL_z \text{sign}(\Delta P)$ . The lateral cell sizes  $L_x$  and  $L_y$  are changed according to the constant volume condition,  $L_x' = L_x/\sqrt{1+\delta}$  and  $L_y' = L_y/\sqrt{1+\delta}$ .

Stage (5) the system is equilibrated again until the pressure components are stabilized during the simulation time  $\Delta\tau + \Delta t + h < t < 2\Delta\tau + \Delta t + h$ .

Stage (6) once a new stable state is reached, then during the  $2\Delta\tau + \Delta t + h < t < 2\Delta\tau + 2\Delta t + h$  simulation time new statistics for  $\bar{P}_i$  are collected and the averages  $\bar{P}_i$  are calculated.

Stage (7) steps (3–6) are repeated over and over again until the resulting system size  $L_z$  stabilizes following the zero difference between the pressure components  $\Delta\bar{P}$ .

Stages (1–7) are schematically drawn in Fig. 12 and explained in the figure caption. The schematic picture illustrates the case of

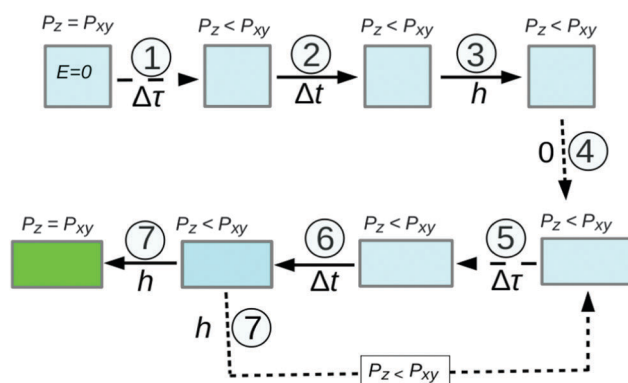


Fig. 12 Schematic representation explaining the simulation stages for getting stabilized composite under the applied field  $E$ . The stages are explained in the text. The squares/rectangles correspond to the un-deformed/deformed composites. The long-dashed arrows (stages 1 and 5) correspond to the system equilibration stages. The full arrows correspond to the stage of gathering necessary statistics for the pressure components. Finally, the short-dashed arrows are for the stage of composite deformation. Above each arrow the number of the corresponding stage is given. Below the arrows the time span of the stage is indicated.

a composite contraction from its initial cubic (a square in 2D drawing) shape to a rectangular prism (a rectangle in 2D drawing) shape.

## Acknowledgements

We thank F. Smallenburg and A. M. Menzel for helpful discussions. E. Allahyarov is thankful for support of this work by Russian Science Foundation (RNF), through the Project No. 14-50-00124. H. Löwen thanks the Deutsche Forschungsgemeinschaft for support of the work through the SPP 1681 on magnetic hybrid materials. L. Zhu acknowledges support by Army Research Office (ARO) under award number W911NF-13-1-0153.

## References

- I. A. Anderson, T. A. Gisby, T. G. McKay, B. M. O'Brien and E. P. Calius, Multi-functional dielectric elastomer artificial muscles for soft and smart machines, *J. Appl. Phys.*, 2012, **112**, 041101.
- F. Carpi, D. De Rossi, R. Kornbluh and R. E. Pelrine, *Dielectric elastomers as electromechanical transducers: fundamentals, materials, devices, models and applications of an emerging electroactive polymer technology*, Elsevier, Oxford, 2008.
- S. Chiba, M. Waki, T. Wada, Y. Hirakawa, K. Masuda and T. Ikoma, Consistent ocean wave energy harvesting using electroactive polymer (dielectric elastomer) artificial muscle generators, *Appl. Energy*, 2013, **104**, 497–502.
- O. Philippova, A. Barabanova, V. Molchanov and A. Khokhlov, Magnetic polymer beads: recent trends and developments in synthetic design and applications, *Eur. Polym. J.*, 2011, **47**, 542–559.
- Ch. A. Grabowski, H. Koerner, J. S. Meth, A. Dang, C. M. Hui, K. Matyjaszewski, M. Bockstaller, M. F. Durstock and R. A. Vaia, Performance of Dielectric Nanocomposites: Matrix-Free, Hairy Nanoparticle Assemblies and Amorphous Polymer-Nanoparticle Blends, *ACS Appl. Mater. Interfaces*, 2014, **6**, 21500–21509.
- P. Brochu and Q. Pei, Advances in dielectric elastomers for actuators and artificial muscles, *Macromol. Rapid Commun.*, 2010, **31**, 10–36.
- Z. Suo, Theory of dielectric elastomers, *Acta Mech. Solida Sin.*, 2010, **23**, 549–578.
- P. Bawa, V. Pillay, Y. E. Choonara and L. C du Toit, Stimuli-responsive polymers and their applications in drug delivery, *Biomed. Mater.*, 2009, **4**, 022001.
- H. Xu, Ch. Wang, Ch. Wang, J. Zoval and M. Madou, Polymer actuator valves toward controlled drug delivery application, *Biosens. Bioelectron.*, 2006, **21**, 2094–2099.
- L. C. Branquinho, M. S. Carria, A. S. Costa, N. Zufelato, M. H. Sousa, R. Miotto, R. Ivkov and A. F. Bakuzis, Effect of magnetic dipolar interactions on nanoparticle heating efficiency: Implications for cancer hyperthermia, *Sci. Rep.*, 2013, **3**, 2887.
- R. E. Newnham, D. P. Skinner and L. E. Cross, Connectivity and piezoelectric-pyroelectric Composites, *Mater. Res. Bull.*, 1978, **13**, 525–536.
- R. E. Newnham, Molecular mechanisms in smart materials, *Mater. Res. Bull.*, 1997, **22**, 20.
- R. Shankar, T. K. Ghosh and R. J. Spontak, Mechanical and actuation behavior of electroactive nanostructured polymers, *Sens. Actuators, A*, 2009, **151**, 46–52.
- P. H. Vargantwar, R. Shankar, A. S. Krishnan, T. K. Ghosh and R. Spontak, Exceptional versatility of solvated block copolymer/ionomer networks as electroactive polymers, *Soft Matter*, 2011, **7**, 1651–1655.
- S. Chiba and M. Waki, in *Extending applications of dielectric elastomer artificial muscles to wireless communication systems. Recent advances in Wireless Communications and Networks*, ed. J. C. Lin, 2011, p. 435.
- R. Pelrine, R. Kornbluh, J. Joseph, R. Heydt, Q. Pei and S. Chiba, High-field electrostriction of elastomeric dielectrics for actuators, *Mater. Sci. Eng., C*, 2000, **11**, 89–100.
- Y. Han, W. Hong and L. E. Faidley, Field-stiffening effect of magneto-rheological elastomers, *Int. J. Solids Struct.*, 2013, **50**, 2281–2288.
- A. Singh, M. Shirolkar, M. V. Limaye, S. Gokhale, C. Khan-Malek and S. K. Kulkarni, A magnetic nano-composite soft polymeric membrane, *Microsyst. Technol.*, 2013, **19**, 409–418.
- B. A. Evans, B. L. Fiser, W. J. Prins, D. J. Rapp, A. R. Shields, D. R. Glass and R. Superfine, A highly tunable silicone-based magnetic elastomer with nanoscale homogeneity, *J. Magn. Magn. Mater.*, 2012, **324**, 501–507.
- B. Sareni, L. Krahenbuhl, A. Beroual and C. Brosseau, Effective dielectric constant of periodic composite materials, *J. Appl. Phys.*, 1996, **80**, 1688–1696.
- T. C. Choy, *Effective Medium Theory*, Oxford, Clarendon Press, 1999, ISBN 978-0-19-851892-1.
- Y. WU, X. Zhao, F. Li and Z. Fan, Evaluation of mixing rules for dielectric constants of composite dielectrics by MC-FEM calculation on 3D cubic lattice, *J. Electroceram.*, 2003, **11**, 227–239.
- F. Deng and K. Van Vliet, Prediction of elastic properties for polymer-particle nanocomposites exhibiting an interphase, *Nanotechnology*, 2011, **22**, 165703.
- S. Y. Fu, X. Q. Feng, B. Lauke and Y. W. Mai, Effects of particle size, particle/matrix interface adhesion and particle loading on mechanical properties of particulate-polymer composites, *Composites, Part B*, 2008, **39**, 933–961.
- A. Upadhyay and R. Singh, Prediction of effective elastic modulus of biphasic composite materials, *Mod. Mech. Eng.*, 2012, **2**, 6–13.
- D. Ivaneyko, V. Toshchevikov, M. Saphiannikova and G. Heinrich, Magneto-sensitive elastomers in a homogeneous magnetic field: a regular rectangular lattice model, *Macromol. Theory Simul.*, 2011, **20**, 411–424.
- D. Ivaneyko, V. Toshchevikov, M. Saphiannikova and G. Heinrich, Effects of particle distribution on mechanical properties of magneto-sensitive elastomers in a homogeneous magnetic field, *Condens. Matter Phys.*, 2012, **15**, 33601.

- 28 D. Ivaneyko, V. Toshchevnikov, M. Saphiannikova and G. Heinrich, Mechanical properties of magneto-sensitive elastomers: unification of the continuum-mechanics and microscopic theoretical approaches, *Soft Matter*, 2014, **10**, 2213–2225.
- 29 A. Yu. Zubarev, On the theory of the magnetic deformation of ferrogels, *Soft Matter*, 2012, **8**, 3174–3179.
- 30 A. Yu. Zubarev, Magneto-deformation of ferrogels and ferroelastomers. Effect of microstructure of the particles spatial disposition, *Physica A*, 2013, **392**, 4824–4836.
- 31 A. Yu. Zubarev and A. S. Elkady, Magnetodeformation and elastic properties of ferrogels and ferroelastomers, *Physica A*, 2014, **413**, 400–408.
- 32 K. Morozov, M. Shliomis and H. Yamaguchi, Magnetic deformation of ferrogel bodies: procrustes effect, *Phys. Rev. E: Stat., Nonlinear, Soft Matter Phys.*, 2009, **79**, 040801.
- 33 Q. M. Zhang, H. Li, M. Poh, F. Xia, Z. Y. Cheng, H. Xu and C. Huang, An all-organic composite actuator material with a high dielectric constant, *Nature*, 2002, **419**, 284.
- 34 C. Huang, Q. M. Zhang, G. deBotton and K. Bhattacharya, All-organic dielectric-percolative three-component composite materials with high electromechanical response, *Appl. Phys. Lett.*, 2004, **84**, 4391.
- 35 C. Huang, Q. M. Zhang, J. Y. Li and M. Rabeony, Colossal dielectric and electromechanical responses in self-assembled polymeric nanocomposites, *Appl. Phys. Lett.*, 2005, **87**, 182901.
- 36 K. Wongtimnoi, B. Guiffard, A. Bogner-Van de Moort, L. Seveyrat, C. Gauthier and J. Y. Cavaille, Improvement of electrostrictive properties of a polyether-based polyurethane elastomer filled with conductive carbon black, *Compos. Sci. Technol.*, 2011, **71**, 885–892.
- 37 M. Roussel, C. Malhaire, A. L. Deman, J. F. Chateaux, L. Petit, L. Seveyrat, J. Galineau, B. Guiffard, C. Segueineau, J. M. Desmarres and J. Martegoutte, Electromechanical study of polyurethane films with carbon black nanoparticles for MEMS actuators, *J. Micromech. Microeng.*, 2014, **24**, 055011.
- 38 S. J. Deshmukh and Z. Ounaies, Single Walled Carbon Nanotube (SWNT)-Polyimide Nanocomposites as Electrostrictive Materials, *Sens. Actuators, A*, 2009, **155**, 246–252.
- 39 B. J. Akle and D. J. Leo, Single-Walled Carbon Nanotubes - Ionic Polymer Electroactive Hybrid Transducers, *J. Intell. Mater. Syst. Struct.*, 2008, **19**, 905–915.
- 40 S. Zhang, N. Zhang, C. Huang, K. Ren and Q. Zhang, Microstructure and electromechanical properties of carbon nanotube/poly(vinylidene fluoride-trifluoroethylenechlorofluoroethylene) composites, *Adv. Mater.*, 2005, **17**, 1897–1901.
- 41 N. Levi, R. Czerw, S. Xing, P. Iyer and D. L. Carroll, Properties of polyvinylidene difluoridecarbon nanotube blends, *Nano Lett.*, 2004, **4**, 1267–1271.
- 42 K. Arlt and M. Wegener, Piezoelectric PZT/PVDF-copolymer 0-3 composites: aspects on film preparation and electrical poling, *IEEE Trans. Dielectr. Electr. Insul.*, 2010, **17**, 1178–1184.
- 43 J. A. Osborn, Demagnetizing factors of the general ellipsoid, *Phys. Rev.*, 1945, **67**, 351–357.
- 44 R. Weeber, S. Kantarovich and C. Holm, Deformation mechanism in 2D magnetic gels studied by computer simulations, *Soft Matter*, 2012, **8**, 9923–9932.
- 45 O. Levy and D. Stroud, Maxwell Garnett theory for mixtures of anisotropic inclusions: Application to conducting polymers, *Phys. Rev. B: Condens. Matter Mater. Phys.*, 1997, **56**, 8035–8046.
- 46 E. Tuncer, Dielectric mixtures: importance and theoretical approaches, *IEEE Elect. Insul. Mag.*, 2013, **29**, 49–58.
- 47 E. Tuncer, S. M. Gubanski and B. Nettelblad, Dielectric relaxation in dielectric mixtures: application of the nite element method and its comparison with mixture formulas, *J. Appl. Phys.*, 2001, **89**, 8092–8100.
- 48 L. Gao and J. Z. Gu, Effective dielectric constant of a two-component material with shape distribution, *J. Phys. D: Appl. Phys.*, 2001, **35**, 267–271.
- 49 A. Einstein, Über die von der molekularkinetischen Theorie der Wärme geforderte Bewegung von in ruhenden Flüssigkeiten suspendierten Teilchen, *Ann. Phys.*, 1905, **17**, 549–560.
- 50 A. Einstein, *Investigation on theory of Brownian motion*, New York, Dover, 1956.
- 51 E. Guth, Theory of filler reinforcement, *J. Appl. Phys.*, 1945, **16**, 20–25.
- 52 W. Kuhn and F. Grün, Beziehungen zwischen elastischen Konstanten und Dehnungsdoppelbrechung hochelastischer Stoffe, *Kolloid Zeitschrift Band*, 1942, **101**, 248–271.
- 53 L. R. G. Treloar, The elasticity and related properties of rubbers, *Rep. Prog. Phys.*, 1973, **36**, 755–826.
- 54 E. I. Arruda and M. C. Boyce, A three-dimensional constitutive model for the large stretch behavior of rubber elastic materials, *J. Mech. Phys. Solids*, 1993, **41**, 389–412.
- 55 P. S. Doyle and E. S. G. Shaqfeh, Dynamic simulation of freely-draining, flexible bead-rod chains: start-up of extensional and shear flow, *J. Non-Newtonian Fluid Mech.*, 1998, **76**, 43–78.
- 56 P. T. Underhill and P. S. Doyle, On the coarse-graining of polymers into bead-spring chains, *J. Non-Newtonian Fluid Mech.*, 2004, **122**, 3–31.
- 57 H. R. Warner, Kinetic theory and rheology of dilute suspensions of finitely extendible dumb-bells, *Ind. Eng. Chem. Fundam.*, 1972, **11**, 379–387.
- 58 M. A. Annunziata, A. M. Menzel and H. Löwen, Hardening transition in a one-dimensional model for ferrogels, *J. Chem. Phys.*, 2013, **138**, 204906.
- 59 G. Pessot, P. Cremer, D. Y. Borin, S. Odenbach, H. Löwen and A. M. Menzel, Structural control of elastic moduli in ferrogels and the importance of non-affine deformations, *J. Chem. Phys.*, 2014, **141**, 124904.
- 60 M. Tarama, P. Cremer, D. Y. Borin, S. Odenbach, H. Löwen and A. M. Menzel, Tunable dynamic response of magnetic gels: impact of structural properties and magnetic fields, *Phys. Rev. E: Stat., Nonlinear, Soft Matter Phys.*, 2014, **90**, 042311.
- 61 M. P. Allen and D. J. Tildesley, *Computer Simulation of Liquids*, Oxford, Clarendon press, 1989.

- 62 Z. Wang, C. Holm. Estimate of the cutoff errors in the Ewald summation for dipolar systems, *J. Chem. Phys.*, 2001, **115**, 6351–6359.
- 63 A. P. Hynninen and M. Dijkstra, Phase behavior of dipolar hard and soft spheres, *Phys. Rev.*, 2005, **72**, 051402.
- 64 B. Groh and S. Dietrich, Crystal structures and freezing of dipolar fluids, *Phys. Rev. E: Stat., Nonlinear, Soft Matter Phys.*, 2001, **63**, 021203.
- 65 R. Tao and J. M. Sun, Three-dimensional structure of induced electrorheological solid, *Phys. Rev. Lett.*, 1991, **67**, 398–401.
- 66 S. Bauer, Poled polymers for sensors and photonic applications, *J. Appl. Phys.*, 1996, **80**, 5531–5558.
- 67 G. S. Neugschwandtner, R. Schwodiauer, S. Bauer-Gogonea, S. Bauer, M. Paajanen and J. Lekkala, Piezo- and pyroelectricity of a polymer-foam space-charge electret, *J. Appl. Phys.*, 2001, **89**, 4503–4511.
- 68 M. Wegener and S. Bauer, Microstorms in Cellular Polymers: A Route to Soft Piezoelectric Transducer Materials with Engineered Macroscopic Dipoles, *ChemPhysChem*, 2005, **6**, 1014–1025.
- 69 M. Wegener, W. Wirges and B. Tiersch, Porous polytetrafluoroethylene (PTFE) electret films: porosity and time dependent charging behavior of the free surface, *J. Porous Mater.*, 2007, **14**, 111–118.
- 70 X. Qui, Patterned piezo-, pyro-, and ferroelectricity of poled polymer electrets, *J. Appl. Phys.*, 2010, **108**, 011101.
- 71 Q. Deng, L. Liu and P. Sharma, Electrets in soft materials: Nonlinearity, size effects, and giant electromechanical coupling, *Phys. Rev. E: Stat., Nonlinear, Soft Matter Phys.*, 2014, **90**, 012603.
- 72 E. Allahyarov, L. Zhu and H. Löwen, Analysis of the actuation properties of charged multilayer films, *J. Appl. Phys.*, 2015, **117**, 034504.
- 73 S. T. Lau, K. W. Kwok, F. G. Shin and S. Kopf, A poling study of lead zirconate titanate/polyurethane 0-3 composites, *J. Appl. Phys.*, 2007, **102**, 044104.
- 74 J. Y. Li, Exchange Coupling in P(VDF-TrFE) Copolymer Based All-Organic Composites with Giant Electrostriction, *Phys. Rev. Lett.*, 2003, **90**, 217601.
- 75 J. Y. Li, L. Zhang and S. Ducharme, Electric energy density of dielectric nanocomposites, *Appl. Phys. Lett.*, 2007, **90**, 132901.
- 76 E. F. Kneller and R. Hawig, The Exchange-Spring Magnet: A New Material Principle for Permanent Magnets, *IEEE Trans. Magn.*, 1991, **27**, 3588–3600.
- 77 M. Doi and S. F. Edwards, *The Theory of Polymer Dynamics*, Clarendon Press, Oxford, U.K., 1986.
- 78 M. Yamamoto, The visco-elastic properties of network structure. II Structural viscosity, *J. Phys. Soc. Jpn.*, 1957, **12**, 1148–1158.
- 79 A. A. Gurtovenko and Y. Ya. Gotlib, Viscoelastic Dynamic Properties of Meshlike Polymer Networks: Contributions of Intra- and Interchain Relaxation Processes, *Macromolecules*, 2000, **33**, 6578–6587.
- 80 J. L. Dote, D. Kivelson and R. N. Schwartz, A molecular quasi-hydrodynamic free-space model for molecular rotational relaxation in liquids, *J. Phys. Chem.*, 1981, **85**, 2169–2180.
- 81 P. P. Bansal and A. J. Ardell, Average nearest-neighbor distances between uniformly distributed finite particles, *Metallography*, 1972, **5**, 97–111.
- 82 D. Levesque and J. J. Weis, Stability of solid phases in the dipolar hard sphere system, *Mol. Phys.*, 2012, **109**, 2747–2756.
- 83 U. Dassanayake, S. Fraden and A. van Blaaderen, Structure of electrorheological fluids, *J. Chem. Phys.*, 2000, **112**, 3851–3858.
- 84 A. P. Hynninen and M. Dijkstra, Phase diagram of dipolar hard and soft spheres: manipulation of colloidal crystal structures by an external field, *Phys. Rev. Lett.*, 2005, **94**, 138303.
- 85 A. Yethiraj and A. van Blaaderen, A colloidal model system with an interaction tunable from hard sphere to soft and dipolar, *Nature*, 2003, **421**, 513–517.
- 86 E. Allahyarov, A. M. Menzel, L. Zhu and H. Löwen, Magneto-mechanical response of bilayered magnetic elastomers, *Smart Mater. Struct.*, 2014, **23**, 115004.